NATIONAL ADVISORY COMMITTEE FOR AERONAUTICS

TECHNICAL NOTE

No. 1474

WIND-TUNNEL INVESTIGATION OF EFFECTS OF UNSYMMETRICAL HORIZONTAL-TAIL ARRANGEMENTS ON POWER-ON STATIC LONGITUDINAL STABILITY OF A SINGLE-ENGINE AIRPLANE MODEL

By Paul E. Purser and Margaret F. Spear

Langley Memorial Aeronautical Laboratory
Langley Field, Va.

Washington

October 1947

NATIONAL ADVISORY COMMITTEE FOR AERONAUTICS

TECHNICAL NOTE NO. 1474

WIND-TUNNEL INVESTIGATION OF EFFECTS OF UNSYMMETRICAL HORIZONTAL-TAIL ARRANGEMENTS ON POWER-ON STATIC LONGITUDINAL STABILITY OF A SINGLE-ENGINE AIRPLANE MODEL

By Paul E. Purser and Margaret F. Spear

SUMMARY

A wind-tunnel investigation has been made to determine the effects of unsymmetrical horizontal-tail arrangements on the power-on static longitudinal stability of a single-engine single-rotation airplane model.

Although the tests and analyses showed that extreme asymmetry in the horizontal tail indicated a reduction in power effects on longitudinal stability for single-engine single-rotation airplanes, the particular "practical" arrangement tested did not show marked improvement. Differences in average downwash between the normal tail arrangement and various other tail arrangements estimated from computed values of propeller-slipstream rotation agreed with values estimated from pitching-moment test data for the flaps-up condition (low thrust and torque) and disagreed for the flaps-down condition (high thrust and torque). This disagreement indicated the necessity for continued research to determine the characteristics of the slipstream behind various propeller-fuselage-wing combinations. Out-of-trim lateral forces and moments of the unsymmetrical tail arrangements that were best from consideration of longitudinal stability were no greater than those of the normal tail arrangement.

INTRODUCTION

The Langley Laboratory of the NACA has undertaken a general study of the problems of stability and control in power-on flight for a model of a single-engine fighter-type airplane.

Up to the present time the study has included a comparison of measured and computed out-of-trim lateral forces and moments induced

by the propeller-slipstream action on the vertical tail on single-engine airplanes (reference 1) and an analysis of the effects of engine skew on the rudder and aileron control required in the take-off and in low-speed power-on flight (unpublished). The study has also included wind-tunnel tests and brief analyses of the effects of unsymmetrical horizontal tails on the power-on static longitudinal stability of single-engine single-rotation airplanes.

The usual power effects on the static longitudinal stability of single-engine single-rotation airplanes may be divided into direct and indirect effects. The direct effects are the forces and the moments acting on the propeller and the downwash resulting from the lift force on the propeller; for constant-power operation these effects are generally destabilizing. The indirect effects are the changes in wing and body forces, moments, and downwash and the changes in tail effectiveness induced by the increased dynamic pressure of the slipstream. The changes in wing and body forces, moments, and downwash may be either stabilizing or destabilizing and the changes in tail effectiveness are usually stabilizing. An additional effect for constant-power operation is that the thrust and torque vary in such a way as to increase the slipstream rotation with increases in lift coefficient. The side of the airplane on which the propeller blade is going up (left side for right-hand rotation), therefore, undergoes an increment of upwash that increases with angle of attack; the opposite side undergoes an increment of downwash that also increases with angle of attack. For the normal horizontal tail the effects of slipstream rotation on longitudinal stability are small. If the tail is unsymmetrical, however, the slipstream rotation possibly can be utilized to change the effects of power-on longitudinal stability. The present paper contains wind-tunnel test data and analyses made to indicate the adjustment in over-all power effects that may be expected from the use of unsymmetrical horizontal tails on single-engine single-rotation airplanes.

COEFFICIENTS AND SYMBOLS

The results of the tests are presented as standard NACA coefficients of forces and moments. Rolling-moment, yawing-moment, and pitching-moment coefficients are given about the center-of-gravity location shown in figure 1 (28.2 percent M.A.C.). The data are referred to the stability axes, which are a system of axes having their origin at the center of gravity and in which the Z-axis is in the plane of symmetry and perpendicular to the relative wind, the X-axis is in the plane of symmetry and perpendicular to the Z-axis, and the Y-axis is perpendicular to the plane of symmetry. The

positive directions of the stability axes, of angular displacements of the airplane and control surfaces, and of hinge moments are shown in figure 2.

The coefficients and symbols are defined as follows:

C_L lift coefficient (Lift/qS)

C_{L_t} tail lift coefficient (L_t/qS)

C_X longitudinal-force coefficient (X/qS)

C_Y lateral-force coefficient. (Y/qS).

C_l rolling-moment coefficient (L/qSb)

C_m pitching-moment coefficient (M/qSc')

C_{m_t} pitching-moment coefficient provided by tail

C_n yawing-moment coefficient (N/qSb)

T_c' effective thrust coefficient based on wing area (T_{eff}/qS)

Q_c torque coefficient $\left(\frac{Q}{\rho V^2 D^3}\right)$

V/nD propeller advance-diameter ratio

η propulsive efficiency $\left(\frac{T_{eff}V}{2\pi nQ}\right)$

Lift = -Z

X longitudinal force, pounds

Y lateral force, pounds

Z vertical force, pounds

L rolling moment, pound-feet

M pitching moment, pound-feet

N yawing moment, pound-feet

L_t lift of isolated horizontal tail, pounds

T_{eff} propeller effective thrust, pounds

Q propeller torque, pound-feet

q free-stream dynamic pressure, pounds per square foot $\left(\frac{\rho V^2}{2}\right)$

q_t effective dynamic pressure at tail, pounds per square foot

S wing area (9.40 sq ft on model)

S_t horizontal-tail area, square feet

c airfoil section chord, feet

$\bar{c}$ average airfoil chord, feet

c' wing mean aerodynamic chord (M.A.C.) (1.31 ft on model)

$$\left(\frac{2}{S}\int_0^{b/2} c^2\, db\right)$$

c_t horizontal-tail mean aerodynamic chord

b wing span (7.509 ft on model)

b_t horizontal-tail span

y/b_t spanwise station of horizontal tail

C_{m_e} pitching-moment coefficient at effective tail-off aerodynamic-center location (zero-lift intercept of tangent to tail-off pitching-moment curve)

l_t tail length measured from neutral point to quarter-chord point of horizontal-tail mean aerodynamic chord

v_t horizontal-tail volume coefficient $\left(\frac{S_t l_t}{Sc'}\right)$

V	air velocity, feet per second
D	propeller diameter (2.27 ft on model)
n	propeller speed, revolutions per second
ρ	mass density of air, slugs per cubic foot
α	angle of attack of thrust line, degrees
α_t	angle of attack of horizontal-tail chord, degrees
ψ	angle of yaw, degrees
ϵ	average angle of downwash, degrees
i_t	angle of stabilizer with respect to thrust line, positive when trailing edge is down, degrees
δ_f	slotted-flap deflection, degrees
δ_{f_p}	plain-flap defloction, degrees
β	propeller blade angle at 0.75 radius (15° on model)
n_o	effective tail-off aerodynamic-center location, percent wing mean aerodynamic chord
n_p	neutral-point location, percent wing mean aerodynamic chord (center-of-gravity location for neutral stability in trimmed flight)

Subscripts:

t	horizontal tail
b	trimmed conditions with center of gravity at neutral point

MODEL AND APPARATUS

Complete Model

The model is a $\frac{1}{5}$-scale model of a 37.5-foot-span single-engine single-rotation airplane. The model has a 30-percent-chord partial-span slotted flap with an internally sealed 10-percent-chord plain

trailing-edge flap, an adjustable stabilizer, and a retractable landing gear. A sketch of a typical section of the flap arrangement used for tests of the model in the landing configuration ($\delta_f = 37^\circ$) is shown in figure 3. The general physical characteristics of the model are given in table I. A three-view drawing and a photograph showing the model mounted in the Langley 7- by 10-foot tunnel are shown in figures 1 and 4, respectively.

The model was equipped with a three-blade, right-hand rotation propeller and a 56-horsepower electric motor. More complete descriptions of the power equipment are given in reference 1.

The model configurations referred to herein are as follows:

δ_f (deg)	δ_{f_p} with respect to slotted flap (deg)	Landing gear	Cowl flap
0	0	Retracted	Closed
37	30	Extended	Open 15°

Flap deflections were set with the aid of templets furnished with the model.

Tail Configurations

In order to obtain relatively extreme indications of the effects of unsymmetrical horizontal-tail configurations, the model was tested with no tail, with the normal horizontal tail (fig. 5(a)), with the right semispan of the normal tail (fig. 5(b)), and with the left semispan of the normal tail (fig. 5(c)). An unsymmetrical arrangement that was thought to be a relatively practical one was devised from two other available horizontal tails having plan forms identical to the normal tail. This arrangement, shown in figure 5(d) and referred to in the text as the asymmetric tail, has approximately one-third of the area on the right and two-thirds on the left, and the total area is about 3 percent greater than that of the normal tail.

Changes in stabilizer setting for all the tails were made with a precision of $\pm 0.1^\circ$ with the aid of a vernier inclinometer.

TESTS

Test Conditions

The following table summarizes the test conditions for the various models:

Model	Dynamic pressure (lb/sq ft)	Test Reynolds number	Air-speed (mph)	Tur-bulence factor	Langley tunnel
Complete; power off and flaps-up power on; $c' = 1.31$ feet	16.37	1,000,000	80	1.60	7- by 10-foot
Complete; flaps-down power on; $c' = 1.31$ feet	9.21	750,000	60	1.60	7- by 10-foot
Isolated asymmetric tail; $\bar{c} = 0.66$ foot	16.37	490,000	80	1.60	7- by 10-foot
Isolated normal tail; $c' = 0.68$ foot	13.00	450,000	71	1.93	4- by 6-foot vertical
Isolated semispan of normal tail; $c' = 0.68$ foot	15.00	490,000	76	1.93	4- by 6-foot vertical

Corrections

Complete model.- All data have been corrected for tares caused by the model support strut. Jet-boundary corrections have been applied to the angles of attack, the longitudinal-force coefficients, and the tail-on pitching-moment coefficients. The corrections were computed as follows by use of reference 2:

$$\Delta\alpha = 1.065C_L$$

$$\Delta C_X = -0.0157C_L^2$$

$$\Delta C_m = -7.74C_L\left(\frac{0.206}{\sqrt{q_t/q}} - 0.116\right)\left(\frac{\partial C_m}{\partial i_t}\right)$$

All jet-boundary corrections were added to the test data.

Tail surfaces.- The data for the isolated normal horizontal tail were corrected for tares caused by the model support strut. The data for the asymmetric tail and the semispan of the normal tail were obtained by tests of the tails mounted on the isolated vertical tail and were approximately corrected for tares by subtracting the data for the vertical tail alone from the data for the combinations tested. The jet-boundary corrections, computed by methods similar to those of reference 3, were added to the angles of attack as follows:

For the normal tail

$$\Delta\alpha_t = 1.59C_{L_t}$$

For the semispan of the normal tail

$$\Delta\alpha_t = 0.91C_{L_t}$$

For the asymmetric tail

$$\Delta\alpha_t = 0.21C_{L_t}$$

Test Procedure for Complete Model

A propeller calibration was made by measuring the longitudinal force of the model with flaps and landing gear retracted and tail off at an angle of attack of 0° for a range of propeller speed. Thrust coefficients were determined from the relation

$$T_c' = C_{X_{\text{propeller operating}}} - C_{X_{\text{propeller removed}}}$$

The torque coefficients were computed by use of a calibration of motor torque as a function of minimum current. The results of the model propeller calibration are presented in figure 6.

All tests of the complete model were made at a dynamic pressure of 16.37 pounds per square foot except power-on tests with flaps deflected, which were made at a dynamic pressure of 9.21 pounds per square foot. This difference was necessitated by power limitations of the model motor.

During the tests the thrust and torque coefficient varied with lift coefficient as shown in figure 7, and the coefficients used corresponded to the values of horsepower shown in figure 8 for

various model scales and airplane wing loadings. The thrust coefficient for the windmilling tests was about -0.02.

RESULTS AND DISCUSSION

Longitudinal-Stability Test Data

Neutral points, determined from the stabilizer test data of figures 9 to 12 by methods outlined in reference 4, are presented in figure 13. Changes in neutral-point location caused by use of power and flaps are presented in figures 14 and 15, respectively. The short-dashed parts of the tail-off and semispan normal-tail curves represent a region of lift where a discontinuity in the pitching-moment curves exists. The discontinuity appears to be a rather common characteristic of wings employing low-drag-type airfoil sections at Reynolds numbers as low as those used in the present tests, and this discontinuity apparently disappears as the Reynolds numbers more nearly approach full-scale values.

The tails should be compared on the basis of equal basic effectiveness $\left(\frac{S_t}{S}\frac{dC_{L_t}}{d\alpha_t}\right)$. The right and left semispans of the normal tail should be compared, therefore, since for each semispan $\frac{S_t}{S}\frac{dC_{L_t}}{d\alpha_t}=0.007$. The normal tail $\left(\frac{S_t}{S}\frac{dC_{L_t}}{d\alpha_t}=0.014\right)$ and the asymmetric tail $\left(\frac{S_t}{S}\frac{dC_{L_t}}{d\alpha_t}=0.013\right)$ form another pair which may be compared.

The curves of figures 13 to 15 show the general trends of the results obtained in the tests, but in order to provide explanations for these trends a discussion based on the various longitudinal-stability parameters shown in the following equation is helpful:

$$n_p = n_o + \frac{\dfrac{V_t \dfrac{dC_{L_t}}{d\alpha_t}\dfrac{q_t}{q}}{C_{L_{\alpha_b}}}\left(1-\dfrac{d\varepsilon}{d\alpha}\right)}{1-\dfrac{\dfrac{d(q_t/q)}{dC_{L_b}}}{\dfrac{q_t/q}{C_{L_b}}}} + \frac{\dfrac{C_{m_e}}{C_{L_b}}}{\dfrac{1}{\dfrac{d(q_t/q)}{dC_{L_b}}\Big/\dfrac{q_t/q}{C_{L_b}}}-1} \qquad (1)$$

This equation is developed and explained in reference 5. The various parameters have been derived by procedures explained in reference 5 from the stabilizer test data of figures 9 to 12 and the isolated-tail data of figure 16. For the sake of brevity, however, curves of these parameters are not presented.

For all conditions the slightly greater stability of the model with the asymmetric tail appears to be caused principally by the tail-effectiveness term of equation (1) since the other two terms are nearly equal for the asymmetric and normal tail arrangements. This greater tail effectiveness must result from the smaller values of effective downwash ϵ and variation of downwash with angle of attack $\frac{d\epsilon}{d\alpha}$ for the asymmetric tail arrangement since the basic tail effectiveness $\left(\frac{S_t}{S}\frac{dC_{L_t}}{d\alpha_t}\right)$ of the asymmetric tail is slightly less than that of the normal tail. For both the propeller-windmilling and power-on cases, the smaller values of ϵ and $\frac{d\epsilon}{d\alpha}$ are probably a result of the spanwise variation of downwash behind the 2:1 tapered wing (reference 6) since analyses presented later show that only small effects of slipstream rotation are to be expected for the particular arrangement used.

With $\delta_f = 0^\circ$ and power on, the markedly greater stability of the model with only the left semispan tail as compared to the model with only the right semispan tail appears to be caused by the tail-effectiveness term of equation (1) since the other two terms of the equation are nearly equal for both semispan tail arrangements. This greater tail effectiveness for the left semispan tail arrangement results from the smaller values of effective downwash ϵ and variation of downwash with angle of attack $\frac{d\epsilon}{d\alpha}$ because of the slipstream rotation. At high lift coefficients the difference between the right and left semispan tail effectiveness is slightly reduced, apparently because of the smaller variation of dynamic-pressure ratio with trim lift coefficient $\frac{d(q_t/q)}{dC_{L_b}}$ obtained in the derivation of the various factors of equation (1) for the left semispan tail. The reduced value of $\frac{d(q_t/q)}{dC_{L_b}}$ is probably caused by a lateral shift of the slipstream at high lift coefficients. This lateral displacement of the slipstream is probably a result of the wing shearing the rotating stream so that the upper part of the slipstream is shifted to the right for right-hand-rotation propellers.

In the power-on flaps-down condition the addition of a horizontal tail on the model was generally destabilizing. For this condition the adverse shift in neutral point caused by the $C_{m_{\dot{\alpha}}}$-term of equation (1) is an important factor in determining neutral-point location so that small values of $\frac{d(q_t/q)}{dC_{L_b}}$ are desirable. A decrease in the value of $\frac{d(q_t/q)}{dC_{L_b}}$, however, also results in a decrease in tail effectiveness. This result was particularly noticeable for the left semispan of the normal tail, and the marked decrease in $\frac{d(q_t/q)}{dC_{L_b}}$ was probably caused by the lateral shift in the slipstream. For this particular model the final result was slightly greater than would be expected from the effects of only slipstream rotation. For other airplanes so designed as to have different values of n_o, $\frac{dC_{L_t}}{d\alpha_t}$, and C_{m_α}, however, the change in $\frac{d(q_t/q)}{dC_{L_b}}$ caused by the lateral shift of the slipstream might produce markedly different results.

The curves of figure 14 show a considerably favorable change in power effects when the left semispan of the normal tail is used rather than the right semispan. The "practical" asymmetric tail, however, did not show a marked improvement when compared with the normal tail. Computations presented in the section entitled "Longitudinal-Stability Computations" agree with the test data in showing little improvement for the asymmetric tail despite the favorable comparison between the right and left semispans of the normal tail.

Longitudinal-Stability Computations

For the four tail arrangements, computations were made of the effects of slipstream rotation on the various longitudinal-stability parameters shown in equation (1). These computations were made in order to provide a check on the validity of quantitative estimates of the adjustment in power effects that may be obtained through utilization of slipstream rotation with unsymmetrical horizontal-tail arrangements. The parameters of equation (1) that are primarily

affected by such tail arrangements are $\frac{d\epsilon}{d\alpha}$, $\frac{S_t}{S}$, $\frac{dC_{L_t}}{d\alpha_t}$, $\frac{q_t}{q}$, and $\frac{d(q_t/q)}{dC_{L_b}}$. For the model considered, the two terms containing q_t are of small importance at low lift coefficients because of the relatively high location of the horizontal tail. Second-order effects such as the changes in the variation with C_{L_b} of l_t, n_o, C_{m_e}, and $C_{L_{\alpha_b}}$ caused by the changes in the neutral-point location were neglected for simplicity, although the effects could be accounted for by use of a series of successive approximations. The procedure used in computing the changes in $\frac{d\epsilon}{d\alpha}$ and n_p are given in the following paragraphs.

Downwash.- The difference in average downwash between the normal tail arrangement and the various other tail arrangements with power on was estimated from the propeller slipstream characteristics by use of references 1 and 7 to 9. Downwash due to the slipstream rotation on each horizontal tail was computed from the following equation:

$$\epsilon_s = \frac{1}{2}\int_0^1 \psi_s \frac{c}{\bar{c}}\, d\left(\frac{y}{b_t}\right) \qquad (2)$$

where ϵ_s is the downwash contributed by the slipstream rotation and ψ_s is the computed angle of twist in the propeller slipstream directly behind the propeller disk. Values on the left (looking forward) were negative since the propeller contributed upwash on the left, and the center lines of the model and the slipstream were assumed to be coincident. The increments in downwash were obtained by subtracting ϵ_s for the various unsymmetrical tails from ϵ_s for the normal tail. A small additional difference of 0.02 between the $\frac{d\epsilon}{d\alpha}$-values for the asymmetric and normal tails, which resulted from differences in spanwise location behind the wing, was calculated from the design charts of reference 6.

The values of the change in downwash due to horizontal-tail arrangements and estimated from the propeller-slipstream characteristics and from the values obtained from the pitching-moment test data are compared in figure 17. The curves remain fairly parallel

where a discrepancy occurs. The displacement of the slipstream at the tail may account for the difference in the initial values at low angles of attack.

Computed values of $\Delta\epsilon$ for the flaps-down condition were much greater than the values obtained from pitching-moment test data. This result was probably caused by the lateral shift in the slipstream associated with the high values of thrust and torque coefficients occurring in the flaps-down condition and which was necessarily neglected in the computations. The shift of the slipstream (reference 1) would be in such a direction as to reduce the previously discussed effects of slipstream rotation.

The agreement of test and computed values of $\Delta\epsilon$ in the flaps-up (low T_c' and Q_c') condition and the disagreement in the flaps-down (high T_c' and Q_c') condition indicate that more research is needed in order to determine the actual characteristics of the slipstream behind various propeller-fuselage-wing combinations.

Dynamic-pressure ratio.- Attempts to estimate the differences among the effective dynamic-pressure ratios for the various tails were unsuccessful. The dynamic-pressure ratios computed from the pitching-moment data presented in figure 18 indicated, however, that such effects actually existed.

Neutral points.- The difference in neutral-point location between the normal and the unsymmetrical tail arrangements was computed as follows:

(a) The various terms of equation (1) were obtained for the normal tail from the test data of figures 9 and 16 by means of procedures outlined in reference 5

(b) Increments of $\frac{d\epsilon}{d\alpha}$ were obtained from figure 17

(c) Values of the various terms of equation (1) for the unsymmetrical tails were obtained by adding the increments of $\frac{d\epsilon}{d\alpha}$ from step (b) to the basic values from step (a) and by considering the changes in tail area and tail lift-curve slope

(d) The resulting values from step (c) were inserted in equation (1) and values of n_p were computed

(e) The increments of n_p were obtained by subtracting the computed values for the unsymmetrical tails from the computed values for the normal tail

The computed changes in n_p and the changes obtained from the test results are compared in figure 19. Agreement between data obtained by the computations and test data is fairly good at low angles of attack despite the fact that the computations neglected changes in q_t/q and $\frac{d(q_t/q)}{dC_{L_b}}$. At high angles of attack where dynamic-pressure effects would be expected to have more influence for the model being considered, disagreement exists between the data obtained by computations and the test data.

Lateral and Directional Trim

Lateral-force and moment coefficients for the model tested with the horizontal-tail configurations at zero yaw are presented in figure 20. Values for the model with the tail off and power on, and values with the normal horizontal tail both windmilling and power on are average values from pitch tests run at $\pm 5^\circ$ yaw. All other measured values are from pitch tests of the model at zero yaw. The values of rolling-moment coefficient at $C_m = 0$ (model trimmed longitudinally) were computed from the pitching-moment data of figures 9 to 12 by the following means: The out-of-trim pitching-moment coefficients were converted to tail loads that were assumed to act at the lateral center of area of the horizontal tail being considered; these tail loads were converted to rolling-moment coefficients by multiplying them by the distance from the center line of the model to the lateral center of area of the tail; and the resulting incremental rolling-moment coefficients were added to the measured values shown in figure 20.

The main fact to be noted is that the unsymmetrical tail arrangements which are best from consideration of longitudinal stability provide out-of-trim lateral forces and moments that are no greater than those provided by the normal tail arrangement.

CONCLUSIONS

The results of wind-tunnel tests of a single-engine single-rotation airplane model equipped with various horizontal-tail arrangements indicated the following conclusions:

1. Although extreme asymmetry in the horizontal tail indicated a reduction in power effects on longitudinal stability the particular "practical" configuration tested did not show marked improvement.

2. Differences in average downwash between the normal tail arrangement and the various other tail arrangements estimated from computed values of propeller-slipstream rotation agreed with values estimated from pitching-moment test data for the flaps-up condition (low thrust and torque) and disagreed for the flaps-down condition (high thrust and torque). This disagreement indicated the necessity for continued research to determine the characteristics of the slipstream behind various propeller-fuselage-wing combinations.

3. Out-of-trim lateral forces and moments of the unsymmetrical tail arrangements that were best from consideration of longitudinal stability were no greater than those of the normal tail arrangement.

Langley Memorial Aeronautical Laboratory
National Advisory Committee for Aeronautics
Langley Field, Va., August 13, 1947

REFERENCES

1. Purser, Paul E., and Spear, Margaret F.: Tests to Determine Effects of Slipstream Rotation on the Lateral Stability Characteristics of a Single-Engine Low-Wing Airplane Model. NACA TN No. 1146, 1946.

2. Gillis, Clarence L., Polhamus, Edward C., and Gray, Joseph L., Jr.: Charts for Determining Jet-Boundary Corrections for Complete Models in 7- by 10-Foot Closed Rectangular Wind Tunnels. NACA ARR No. L5G31, 1945.

3. Swanson, Robert S., and Schuldenfrei, Marvin J.: Jet-Boundary Corrections to the Downwash behind Powered Models in Rectangular Wind Tunnels with Numerical Values for 7- by 10-Foot Closed Wind Tunnels. NACA ARR, Aug. 1942.

4. Schuldenfrei, Marvin: Some Notes on the Determination of the Stick-Fixed Neutral Point from Wind-Tunnel Data. NACA RB No. 3I20, 1943.

5. Wallace, Arthur R., Rossi, Peter F., and Wells, Evalyn G.: Wind-Tunnel Investigation of the Effect of Power and Flaps on the Static Longitudinal Stability Characteristics of a Single-Engine Low-Wing Airplane Model. NACA TN No. 1239, 1947.

6. Silverstein, Abe, and Katzoff, S.: Design Charts for Predicting Downwash Angles and Wake Characteristics behind Plain and Flapped Wings. NACA Rep. No. 648, 1939.

7. Stickle, George W., and Crigler, John L.: Propeller Analysis from Experimental Data. NACA Rep. No. 712, 1941.

8. Crigler, John L.: Comparison of Calculated and Experimental Propeller Characteristics for Four-, Six-, and Eight-Blade Single-Rotating Propellers. NACA ACR No. 4B04, 1944.

9. Crigler, John L., and Talkin, Herbert W.: Charts for Determining Propeller Efficiency. NACA ACR No. L4I29, 1944.

TABLE I

MODEL WING AND TAIL-SURFACE DATA

	Wing	Horizontal tail semispan			Vertical tail
		Small	Normal	Large	
Area, sq ft	9.40	0.718	1.075	1.494	[a]1.25
Span, ft	7.509	1.36	1.67	1.96	1.335
Aspect ratio	6.00	2.58	2.58	2.58	1.30
Taper ratio	2.00	1.79	1.79	1.79	
Dihedral of chord plane, deg Inboard panel Outboard panel	 -0.73 7.72	0	0	0	
Sweepback, quarter chord line, deg	0				
Root section	NACA 66(215)-216	NACA 65(216)-015.4 modified[b]	NACA 65(216)-015.4 modified[b]	NACA 65(216)-015.4 modified[b]	NACA 64,2-015 modified[b]
Break section	NACA 66(215)-216				
Tip section	NACA 66(215)-216	NACA 65(216)-012 modified[b]	NACA 65(216)-012 modified[b]	NACA 65(216)-012 modified[b]	NACA 64(215)-012 modified[b]
[c]Angle of incidence at root, deg	0				
[c]Angle of incidence at break, deg	0				
[c]Angle of incidence at tip, deg	0				
M.A.C., ft	1.31	0.56	0.68	0.803	1.03
Root chord, ft	1.68	0.69	0.84	0.995	1.35
Theoretical tip chord, ft	0.84	0.39	0.47	0.556	0.59

[a]Includes no dorsal fin area.
[b]Trailing edge cusp removed.
[c]Angle of incidence measured with respect to thrust line.

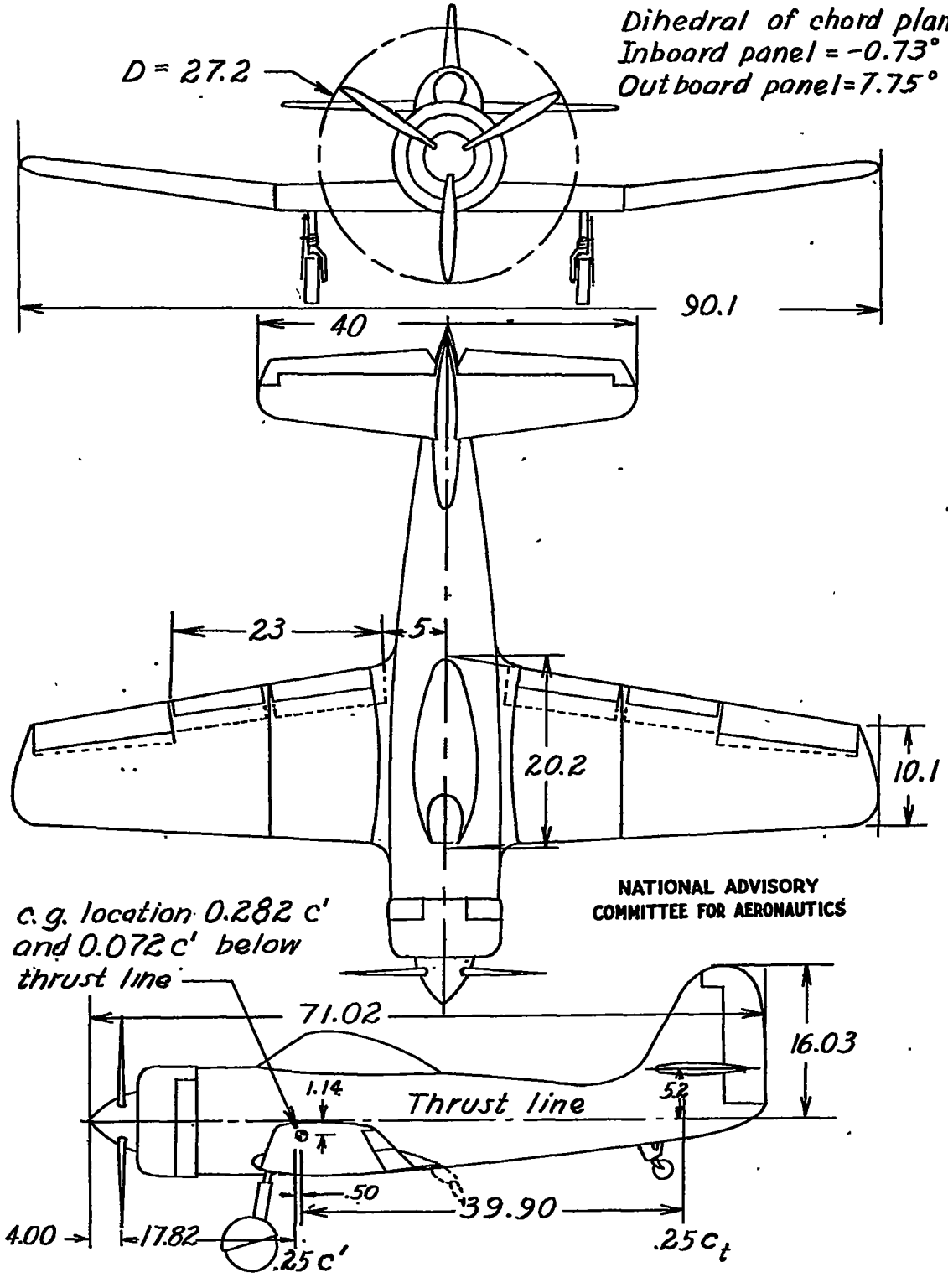

Figure 1.- Three-view drawing of $\frac{1}{5}$-scale model showing normal tail. All dimensions in inches.

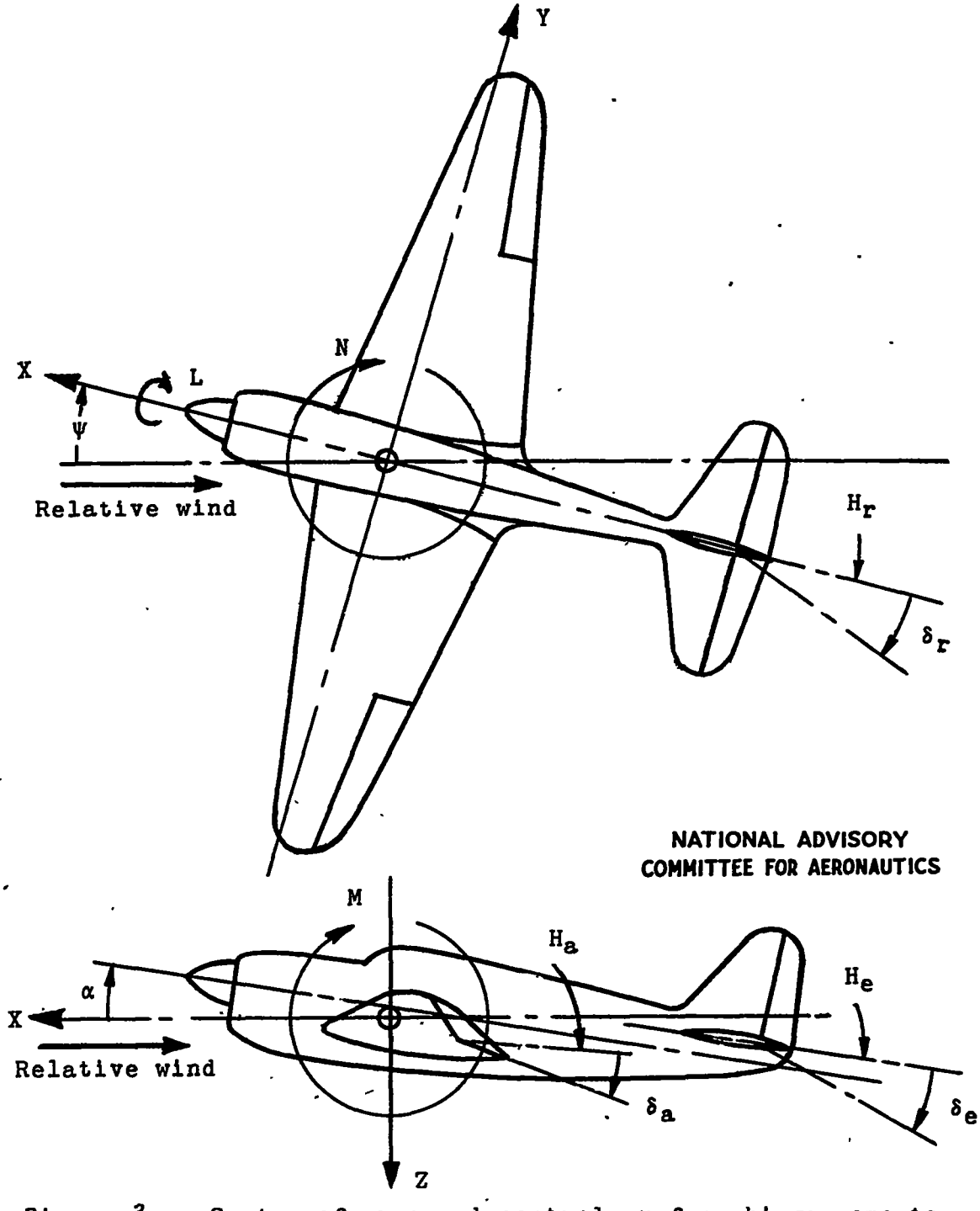

Figure 2 .- System of axes and control-surface hinge moments and deflections. Positive values of forces, moments, and angles are indicated by arrows. Positive values of tab hinge moments and deflections are in the same directions as the positive values for the control surfaces to which the tabs are attached.

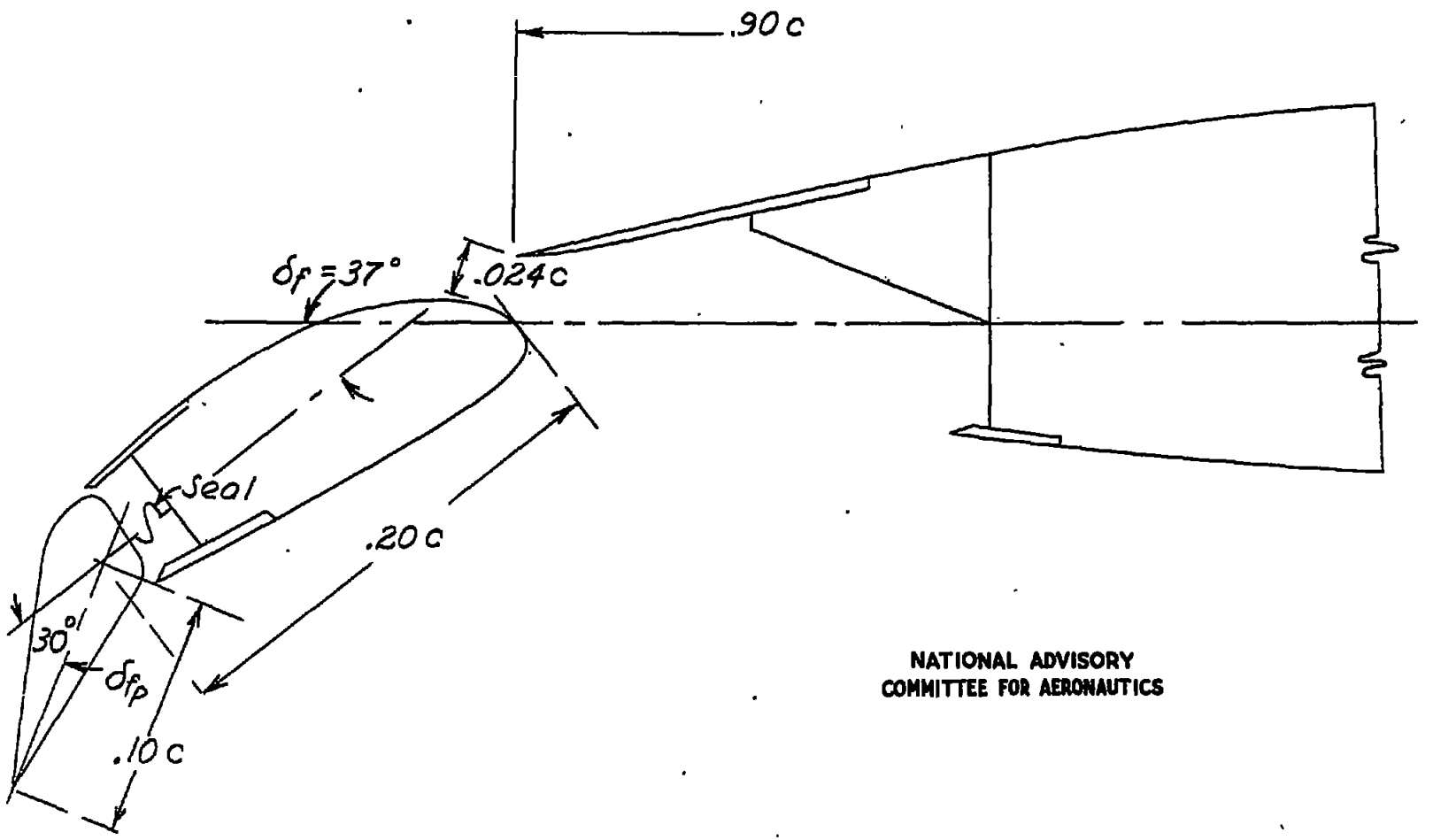

Figure 3. - Typical section of slotted-and plain-flap arrangement used for tests of the model in the landing condition.

Figure 4.- Photograph of the single-engine airplane with normal tail mounted in the Langley 7- by 10-foot tunnel.

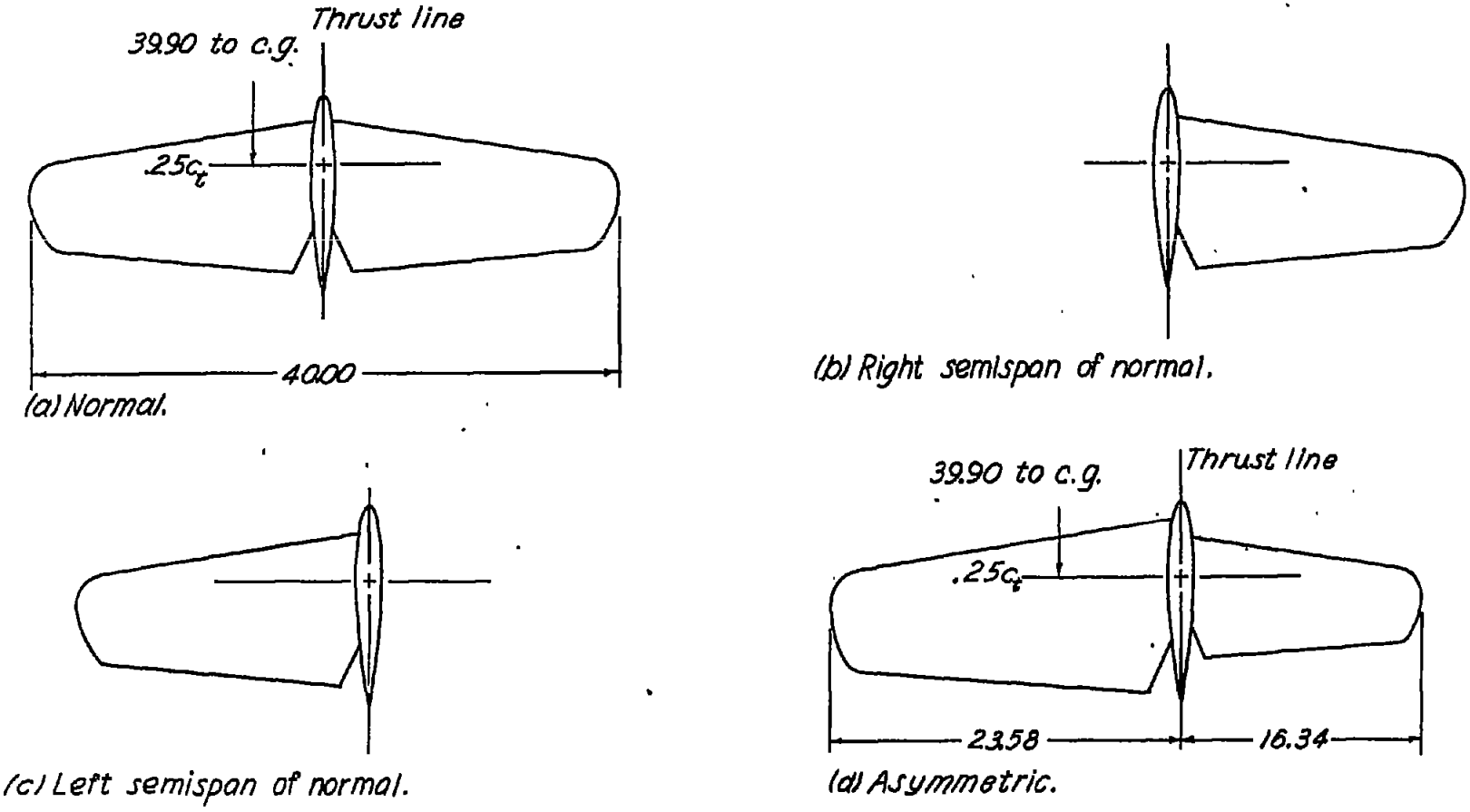

Figure 5.- Plan view of the horizontal tails tested. All dimensions in inches.

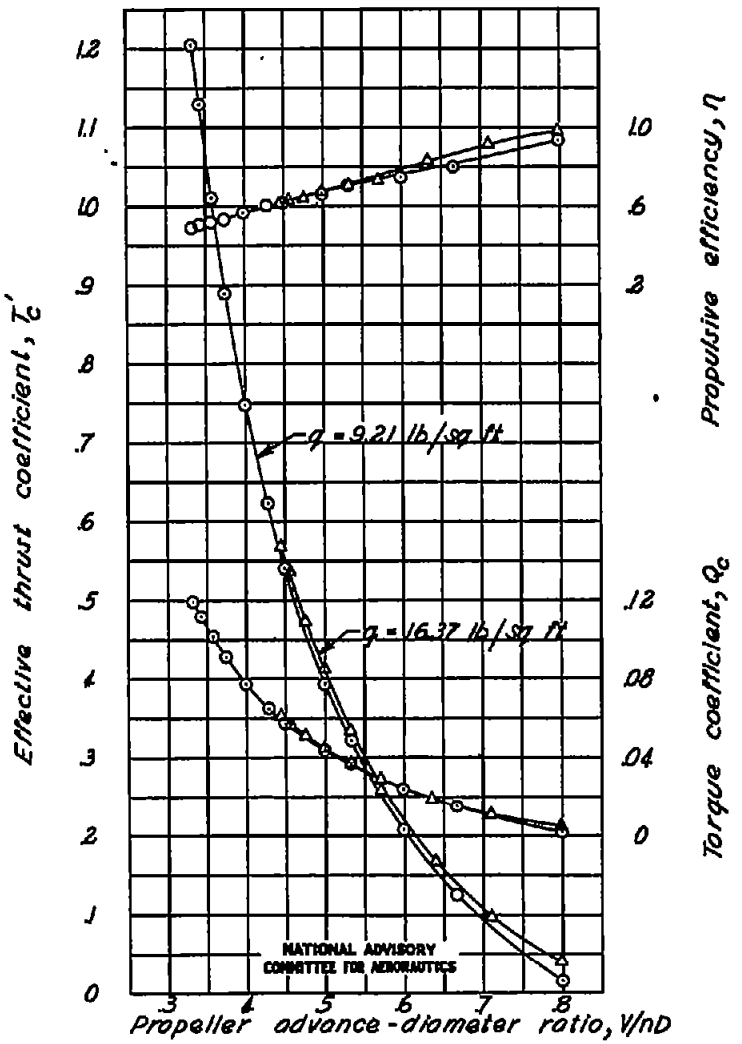

Figure 6.- Propeller calibration of the single-engine airplane model. $\delta_f = 0°$; $\alpha = 0°$; $\beta = 15°$; D = 2.27 feet.

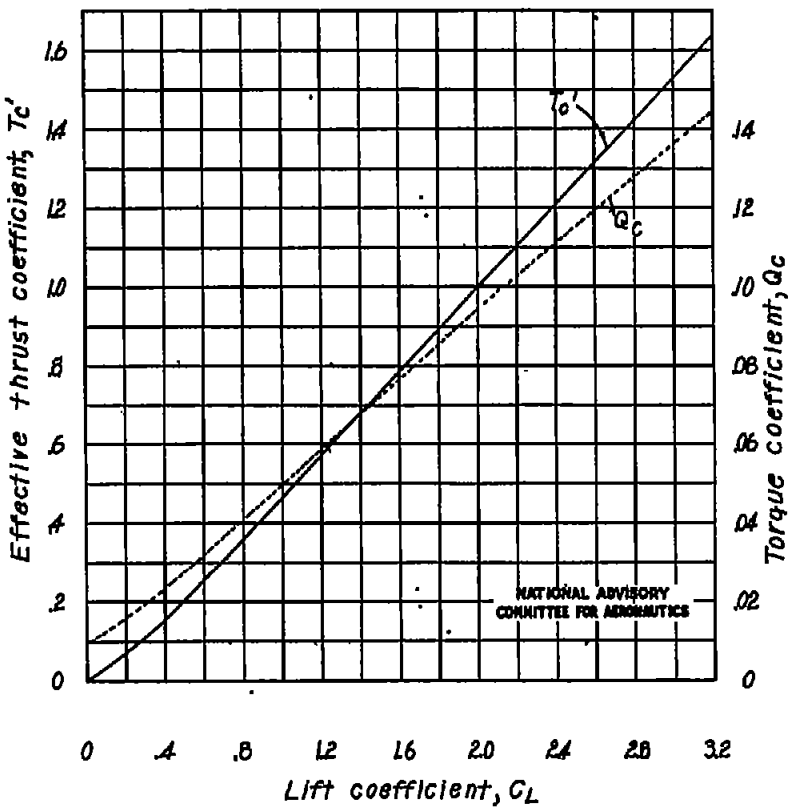

Figure 7.- Thrust and torque coefficient for the single-engine airplane model.

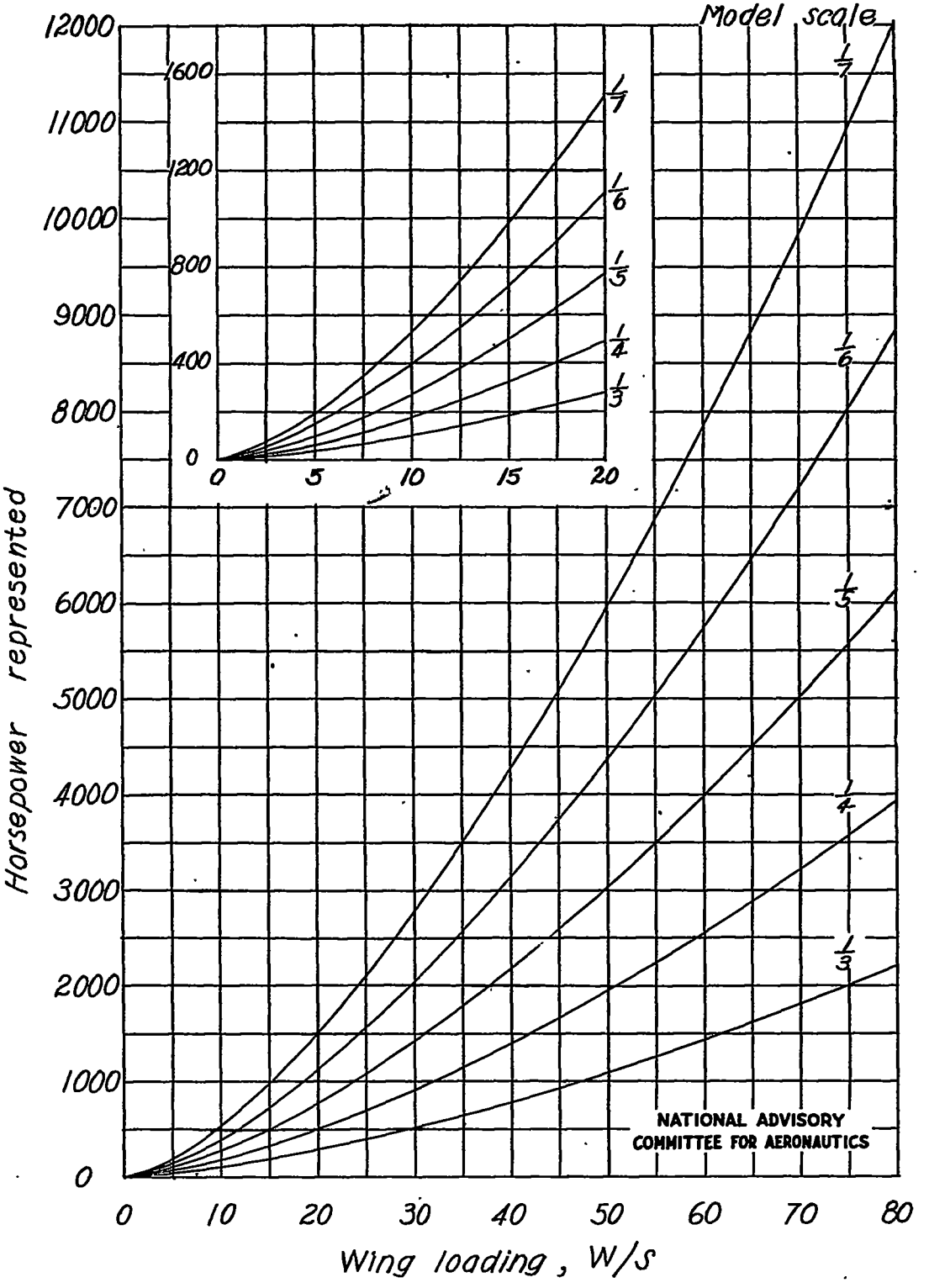

Figure 8.- Horsepower represented for various wing loadings and model scales.

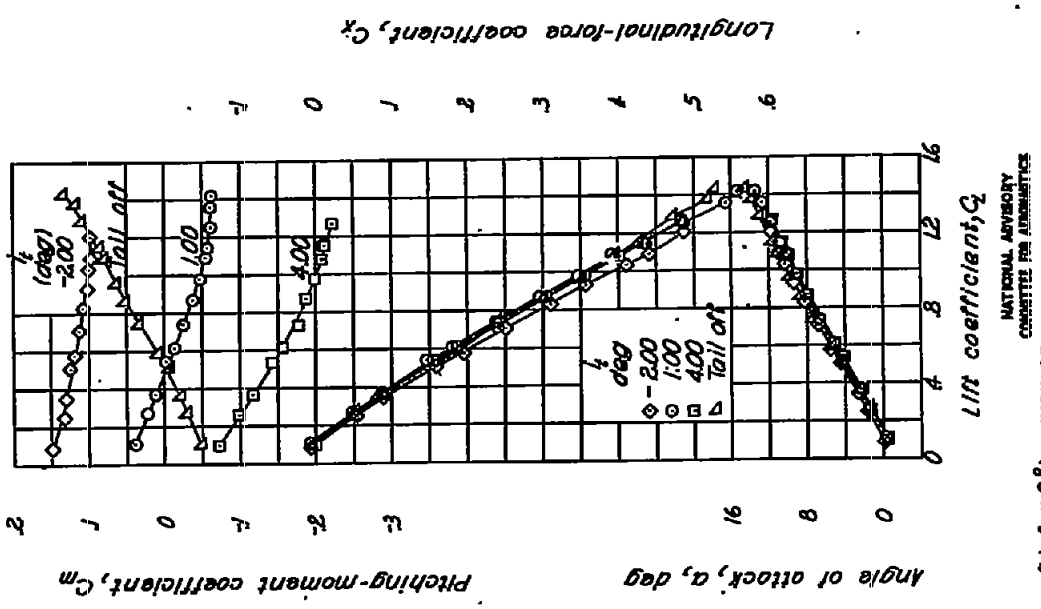

(b) $\phi_p = 0°$; power on.

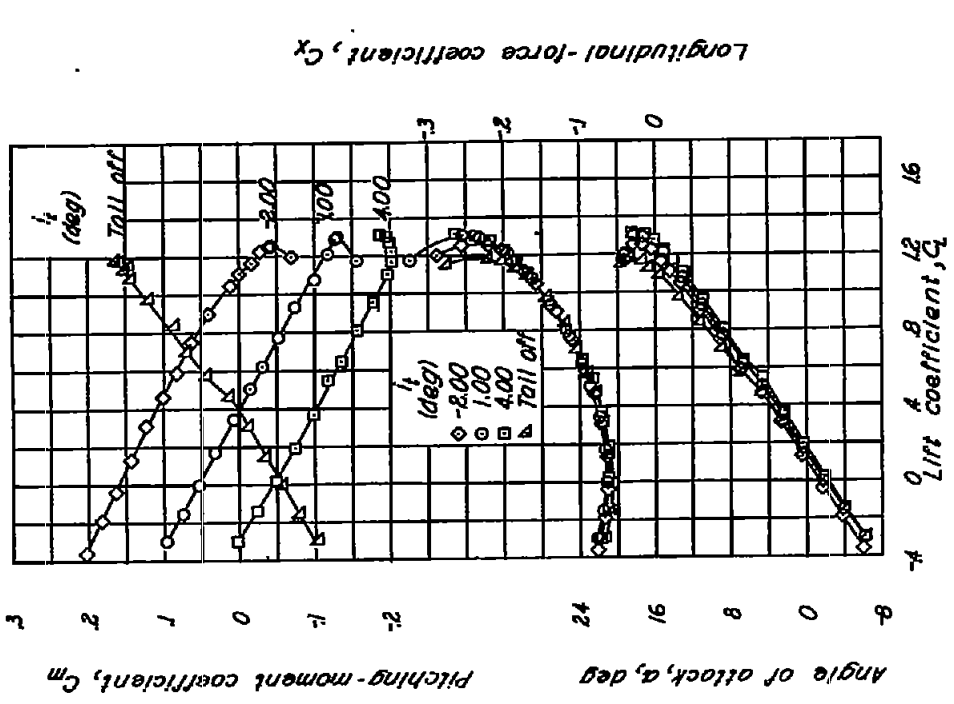

(a) $\phi_p = 0°$; windmilling propeller.

Figure 9.- Effect of the normal horizontal tail on the longitudinal characteristics of the single-engine airplane model.

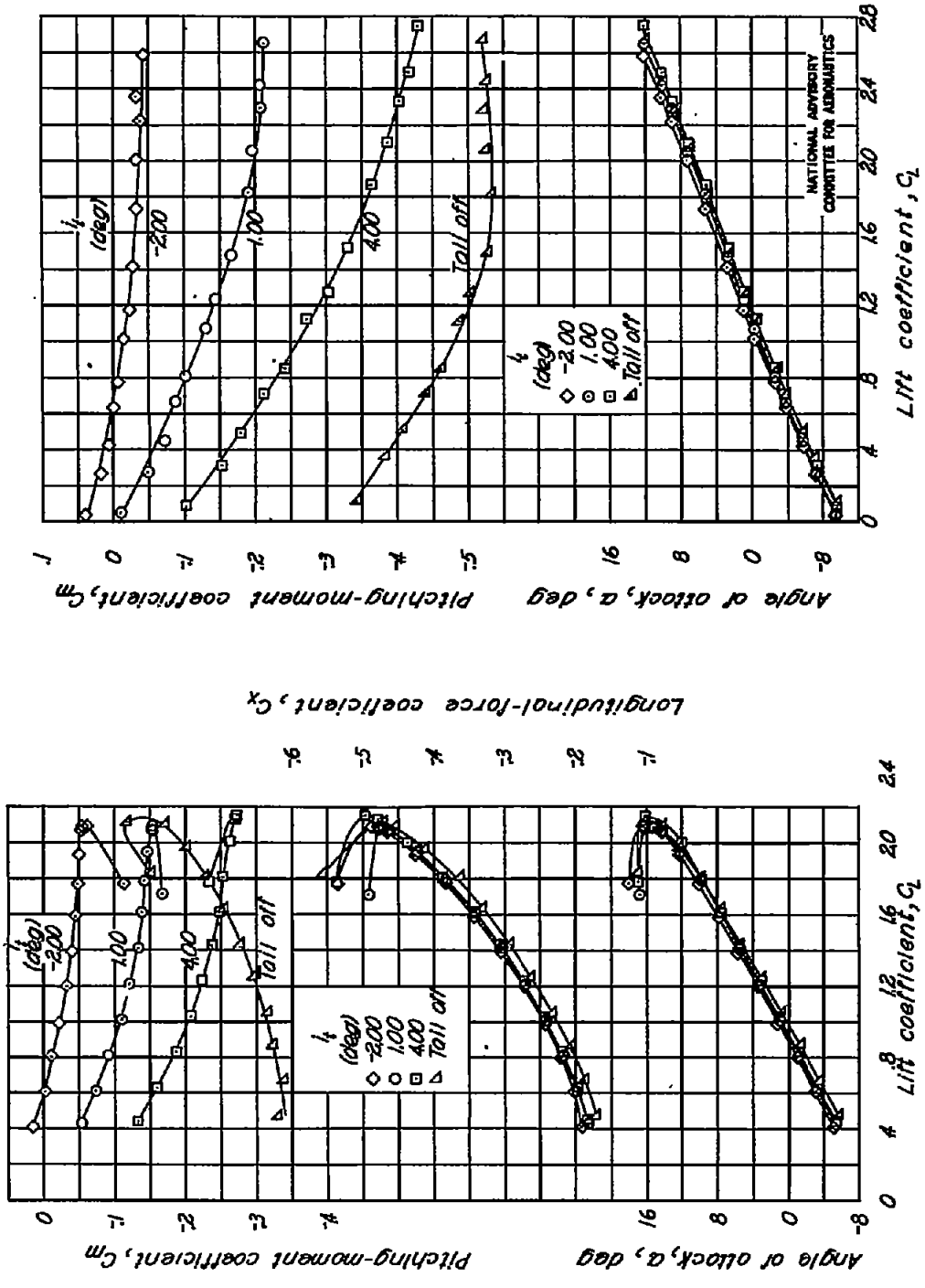

(a) $\delta_f = 37°$; power on.

(c) $\delta_f = 37°$; windmilling propeller.

Figure 9.- Continued.

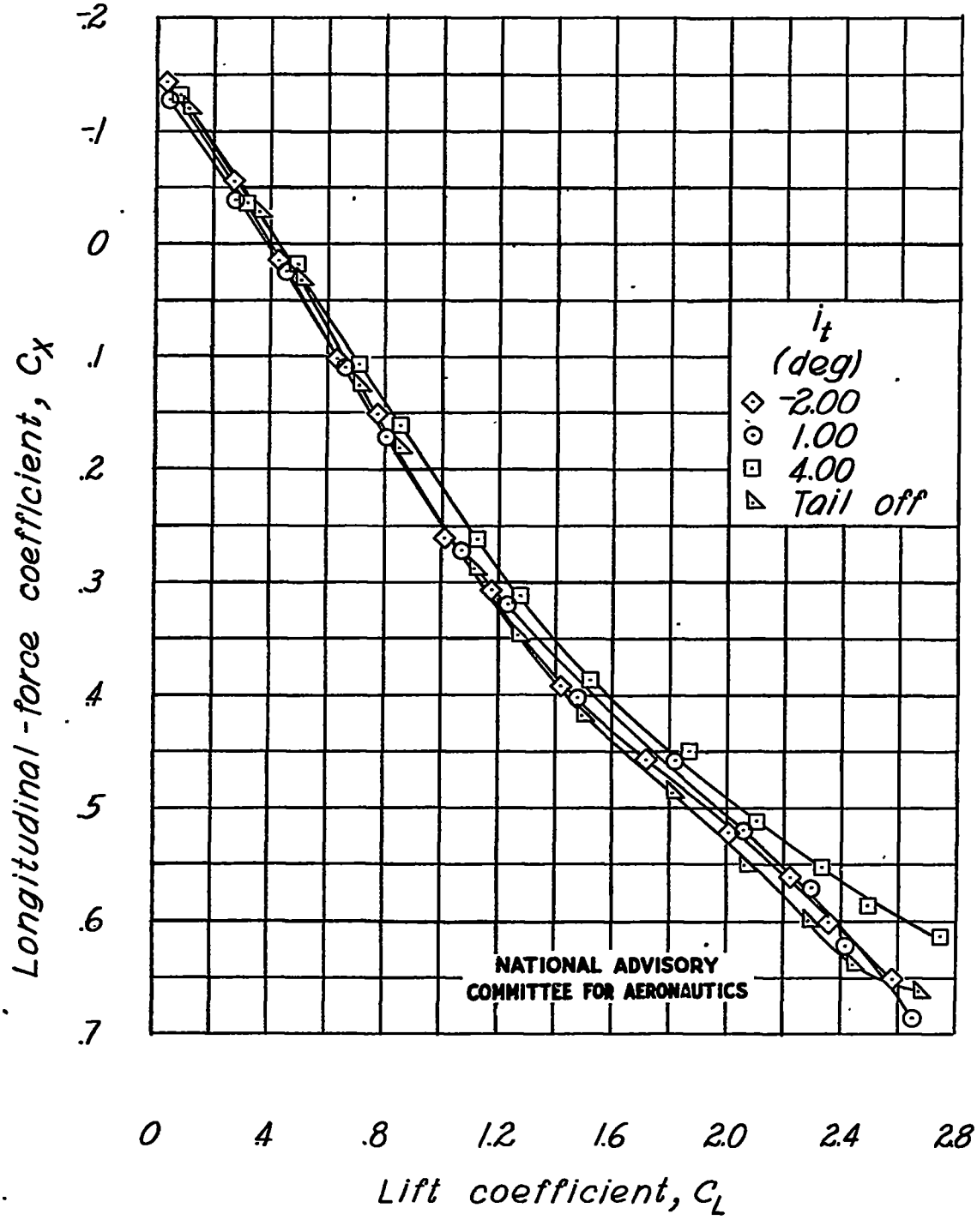

(d) Concluded.

Figure 9.- Concluded.

Figure 10. — Effect of the right semispan of the normal horizontal tail on the longitudinal characteristics of the single-engine airplane model.

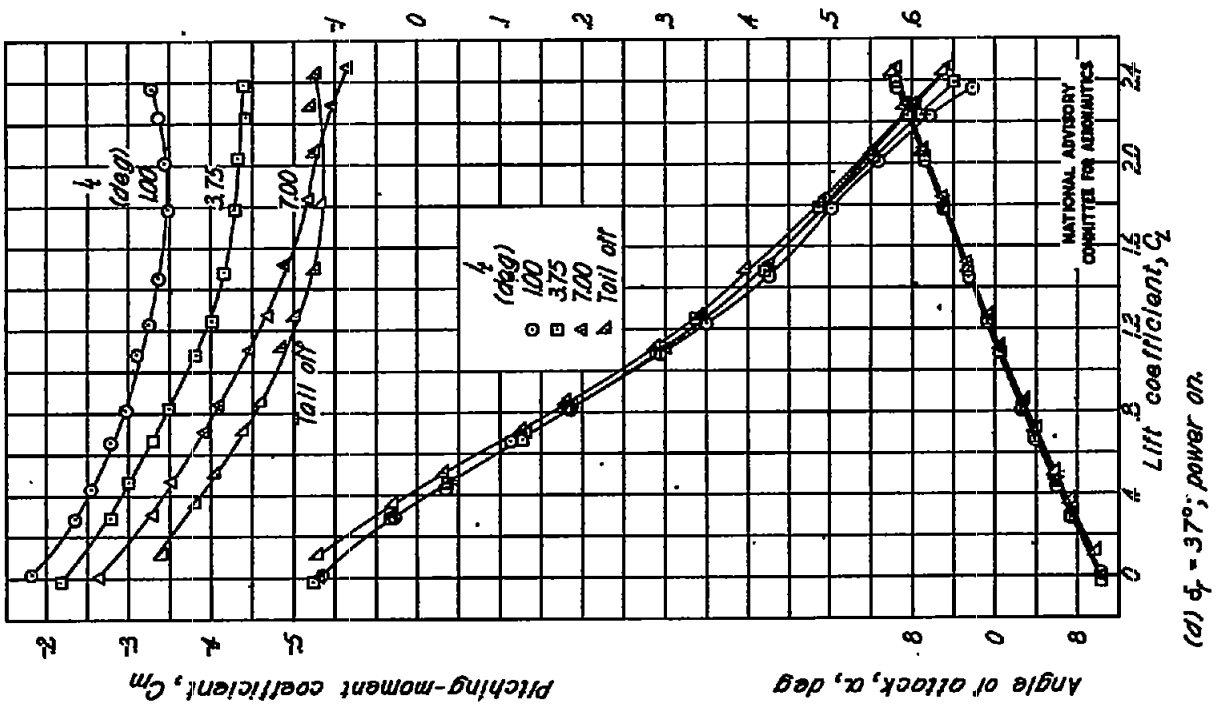

(d) $\delta_f = 37°$; power on.

Figure 10.-Concluded.

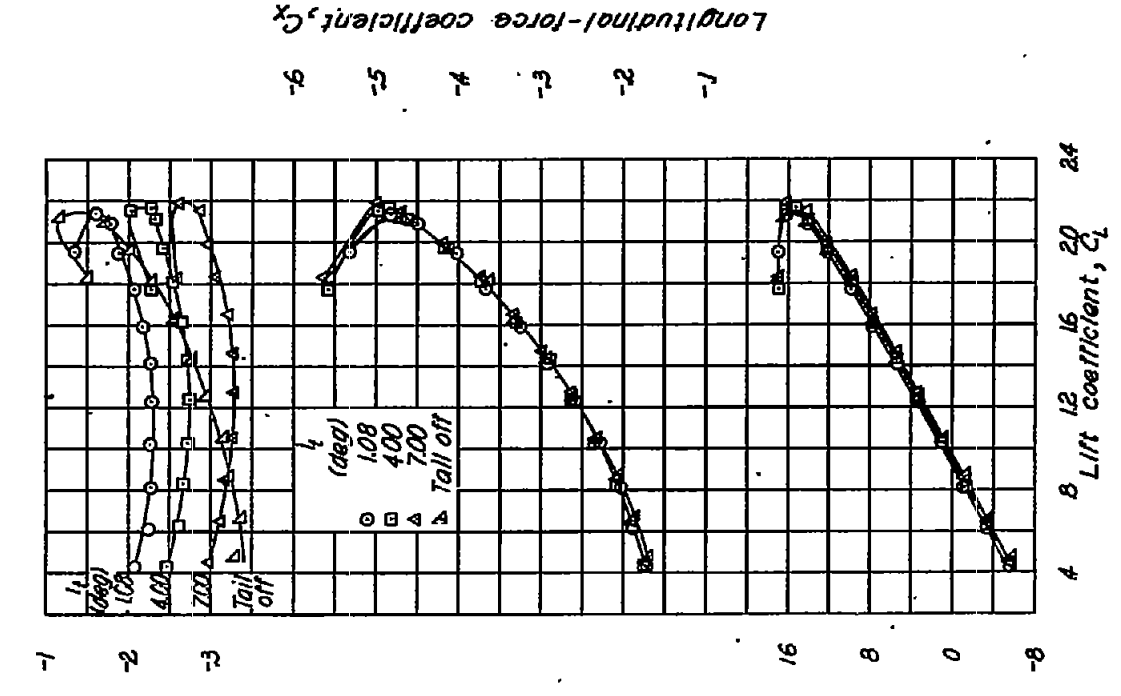

(c) $\delta_f = 37°$; windmilling propeller.

(a) $\delta_f = 0°$; windmilling propeller.

(b) $\delta_f = 0°$; power on.

NATIONAL ADVISORY COMMITTEE FOR AERONAUTICS

Figure 11.— Effect of the left semispan of the normal horizontal tail on the longitudinal characteristics of the single-engine airplane model.

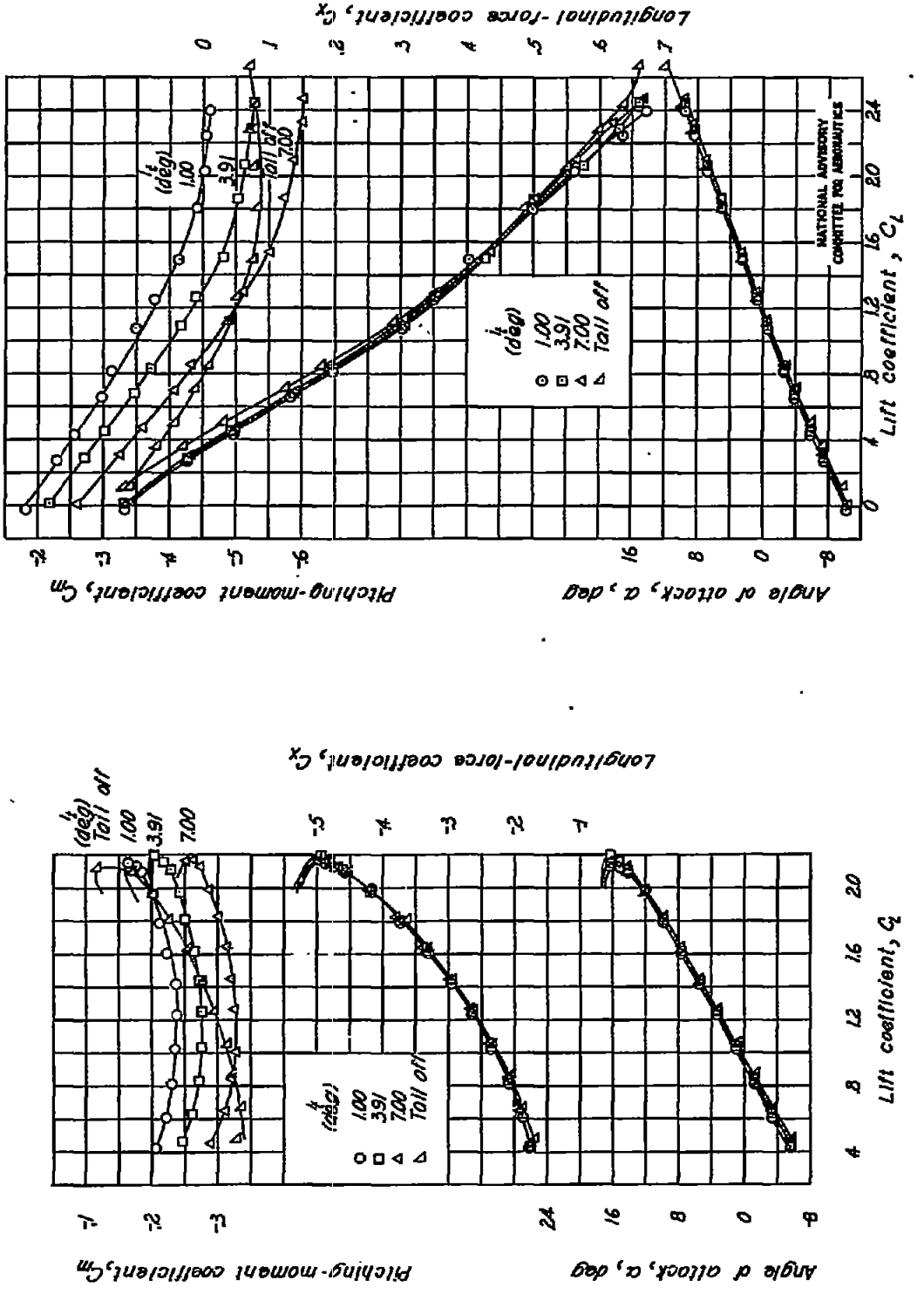

(a) $\delta_f = 37°$; windmilling propeller.

(d) $\delta_f = 37°$; power on.

Figure 11.- Concluded.

(a) $\delta_f = 0°$; windmilling propeller.

(b) $\delta_f = 0°$; power on.

NATIONAL ADVISORY COMMITTEE FOR AERONAUTICS

Figure 12.— Effect of the asymmetric horizontal tail on the longitudinal characteristics of the single-engine airplane model.

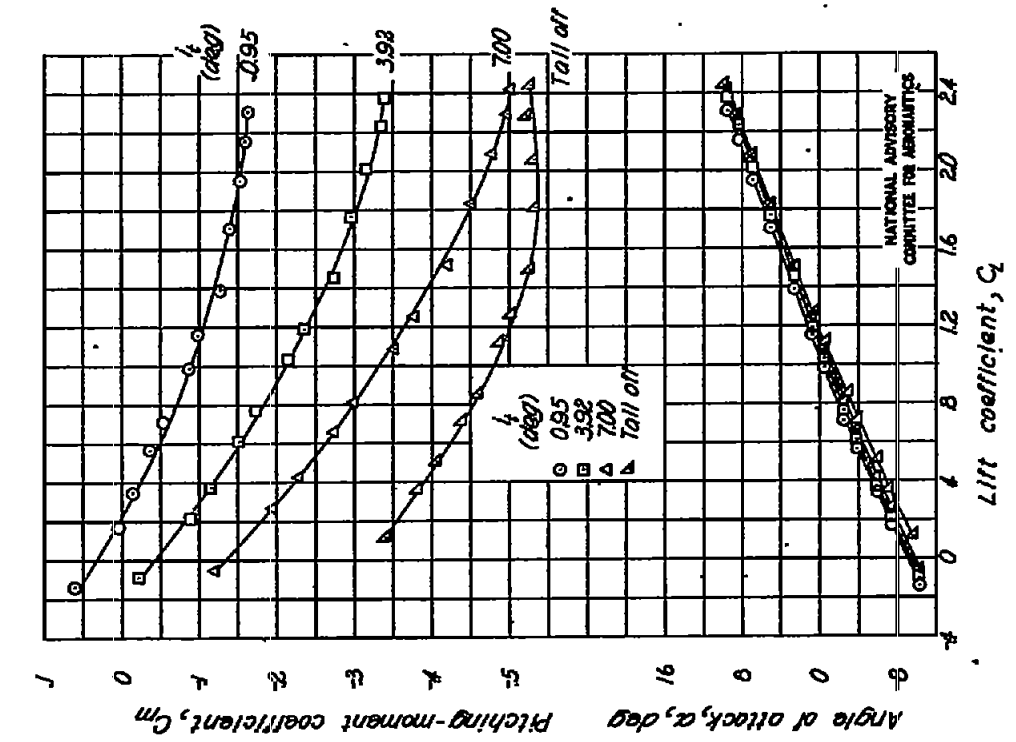

(a) δ_f = 37°; power on.

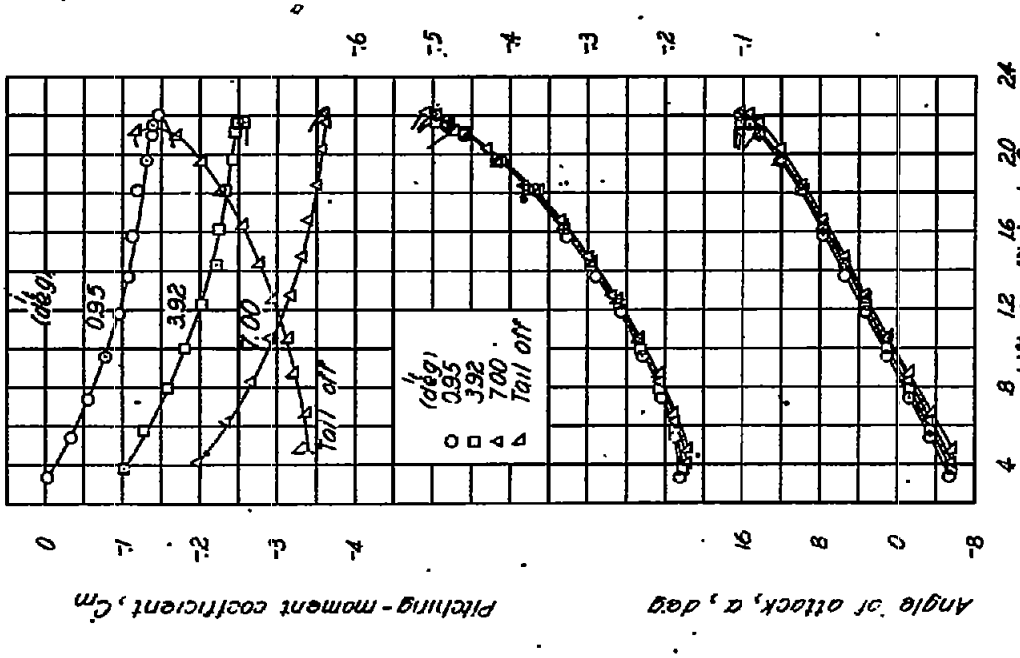

(c) δ_f = 37°; windmilling propeller.

Figure 42 - Continued

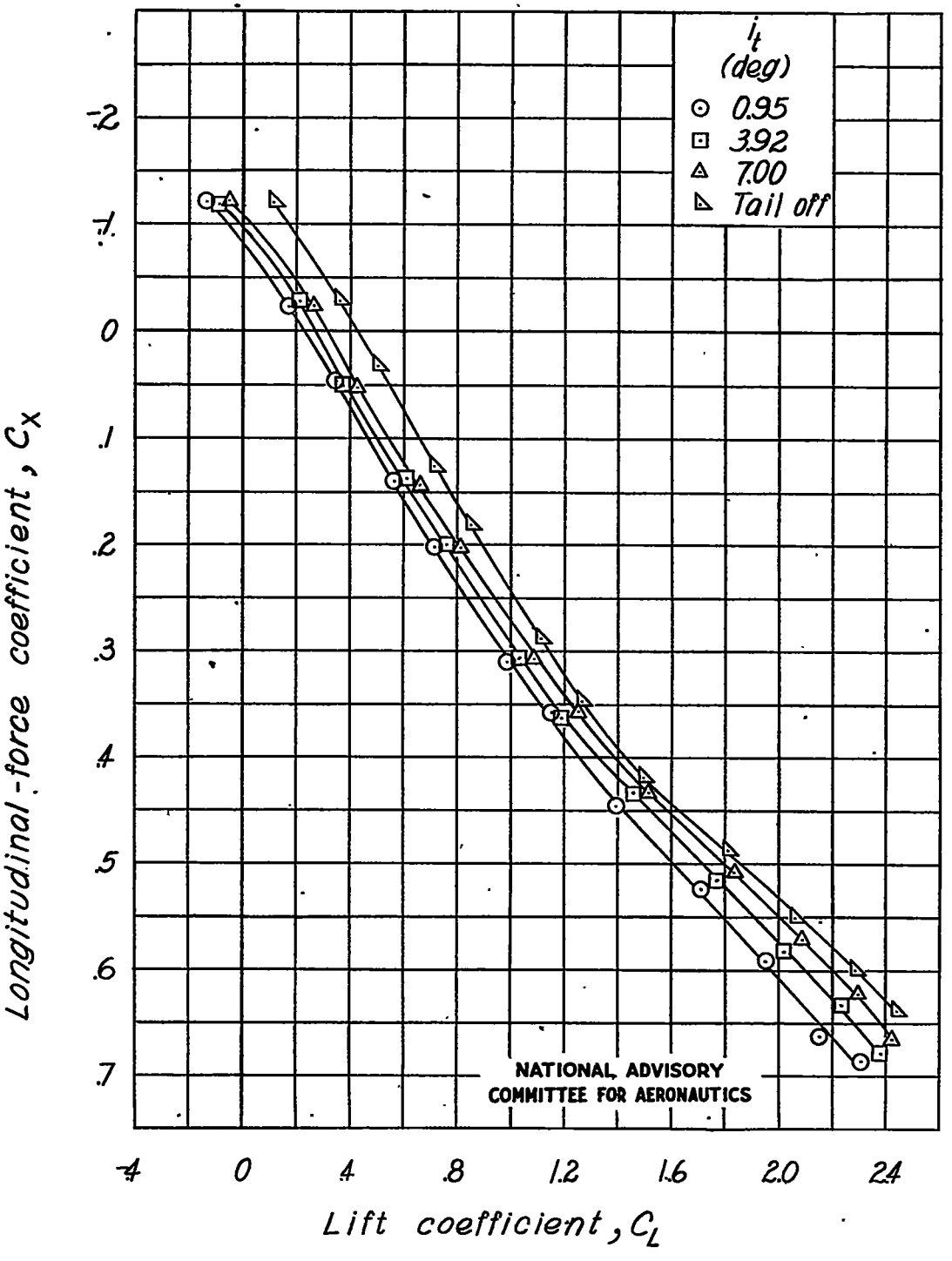

(d) Concluded.

Figure 12.- Concluded.

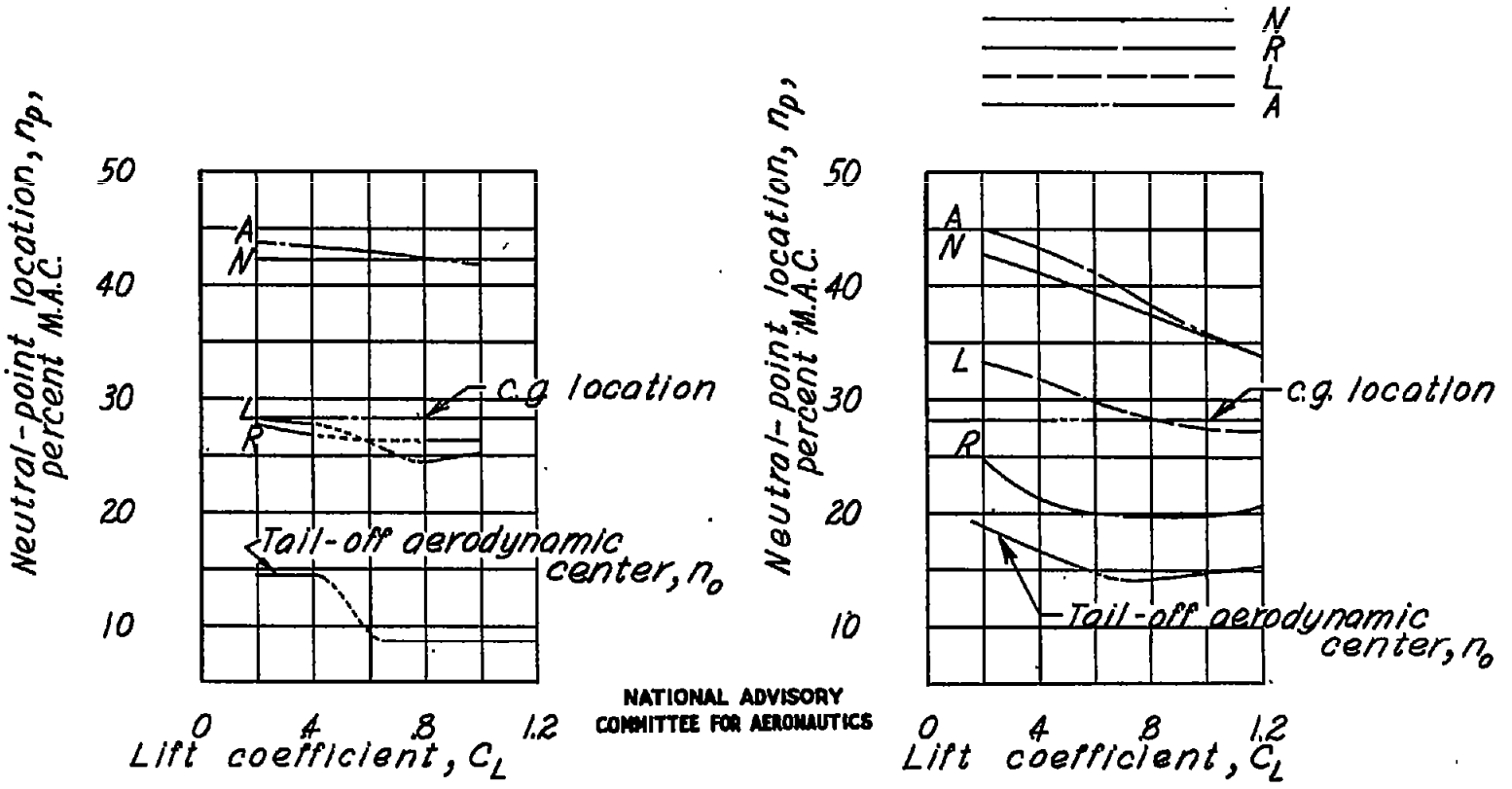

(a) $\delta_f = 0°$; windmilling propeller.

(b) $\delta_f = 0°$; power on.

Figure 13.— The effect of horizontal-tail arrangements on the neutral-point location of the single-engine airplane model. N, normal tail; L, left semispan of normal tail; R, right semispan of normal tail; A, asymmetric tail.

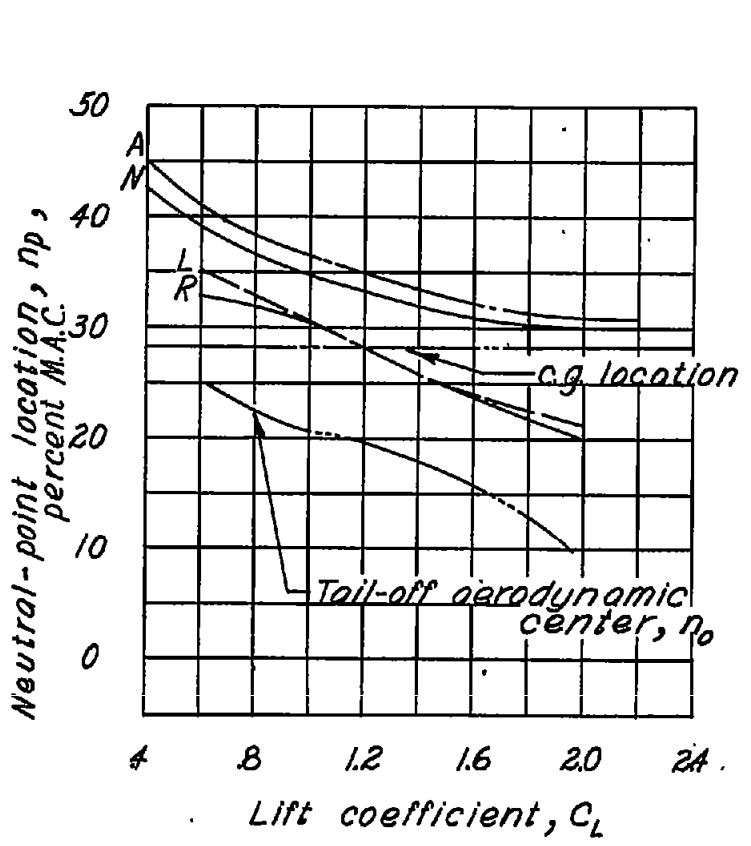

(c) δ_f = 37°; windmilling propeller.

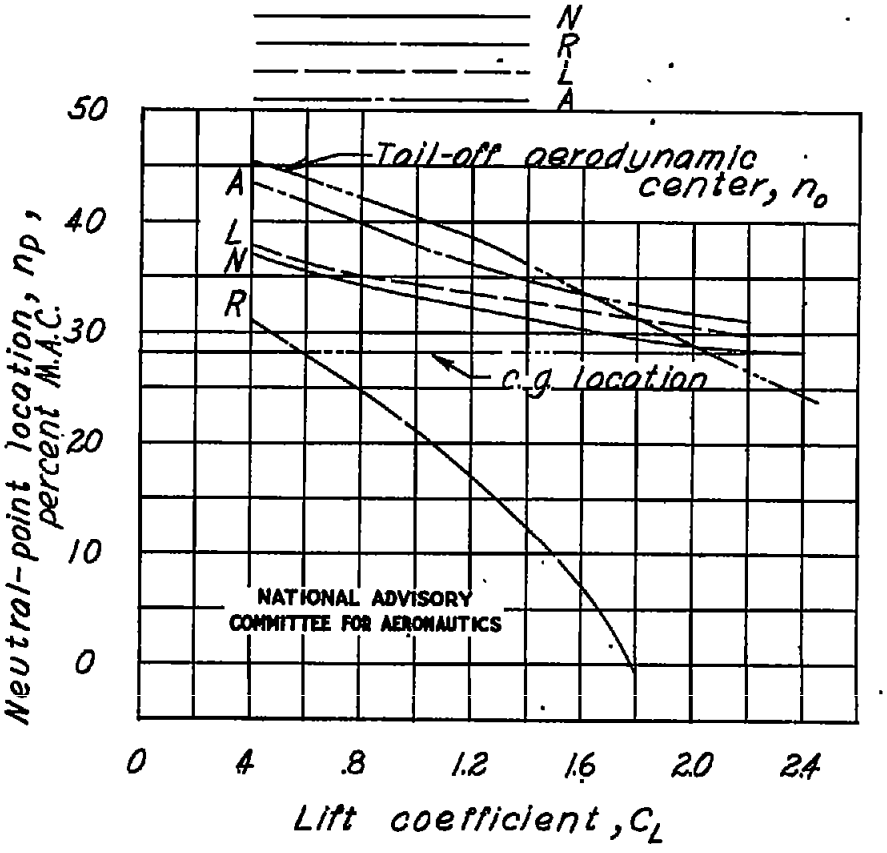

(d) δ_f = 37°; power on.

Figure 13.- Concluded.

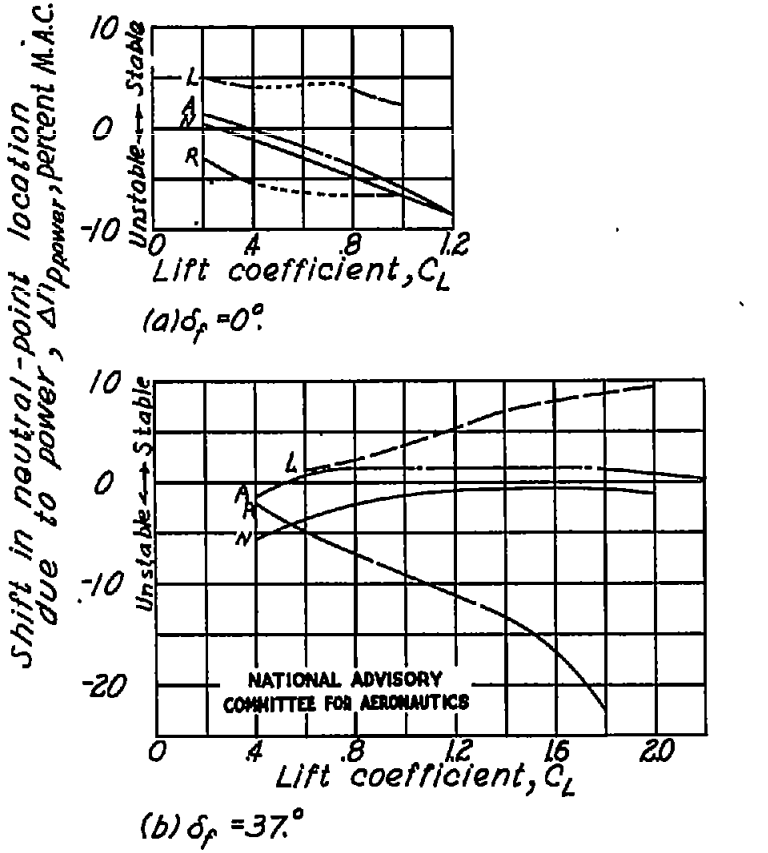

Figure 14. — The effect of unsymmetrical horizontal tails on the shift in neutral-point location due to power of the single-engine airplane model.
$\Delta n_{P_{power}} = n_{P_{power\ on}} - n_{P_{windmilling\ propeller}}$; N, normal tail; L, left semispan of normal tail; R, right semispan of normal tail; A, asymmetric tail.

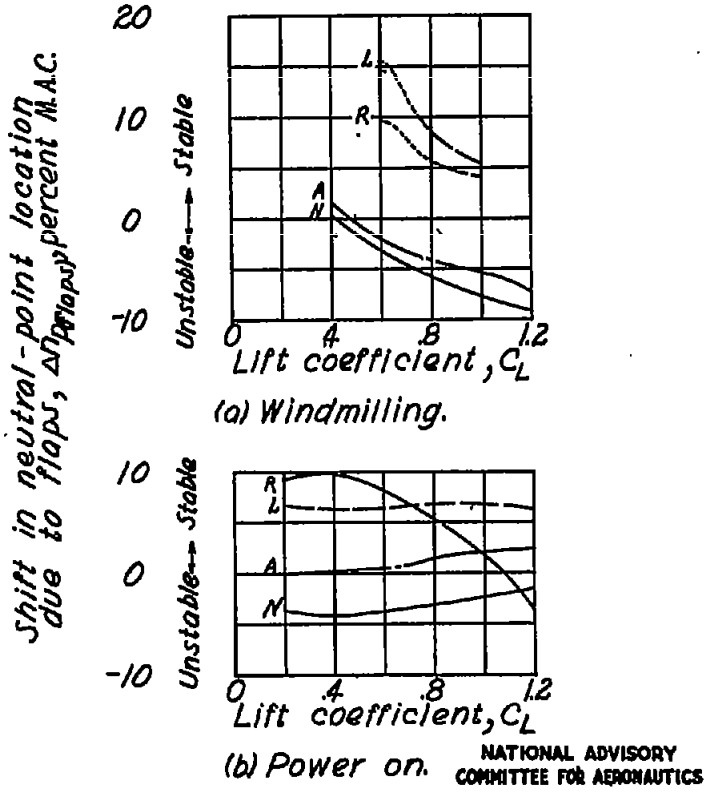

Figure 15. — The effect of unsymmetrical horizontal tails on the shift in neutral-point location due to flaps of the single-engine airplane model.
$\Delta n_{P_{(flaps)}} = n_{P_{\delta_f = 37°}} - n_{P_{\delta_f = 0°}}$; N, normal tail; L, left semispan of normal tail; R, right semispan of normal tail; A, asymmetric tail.

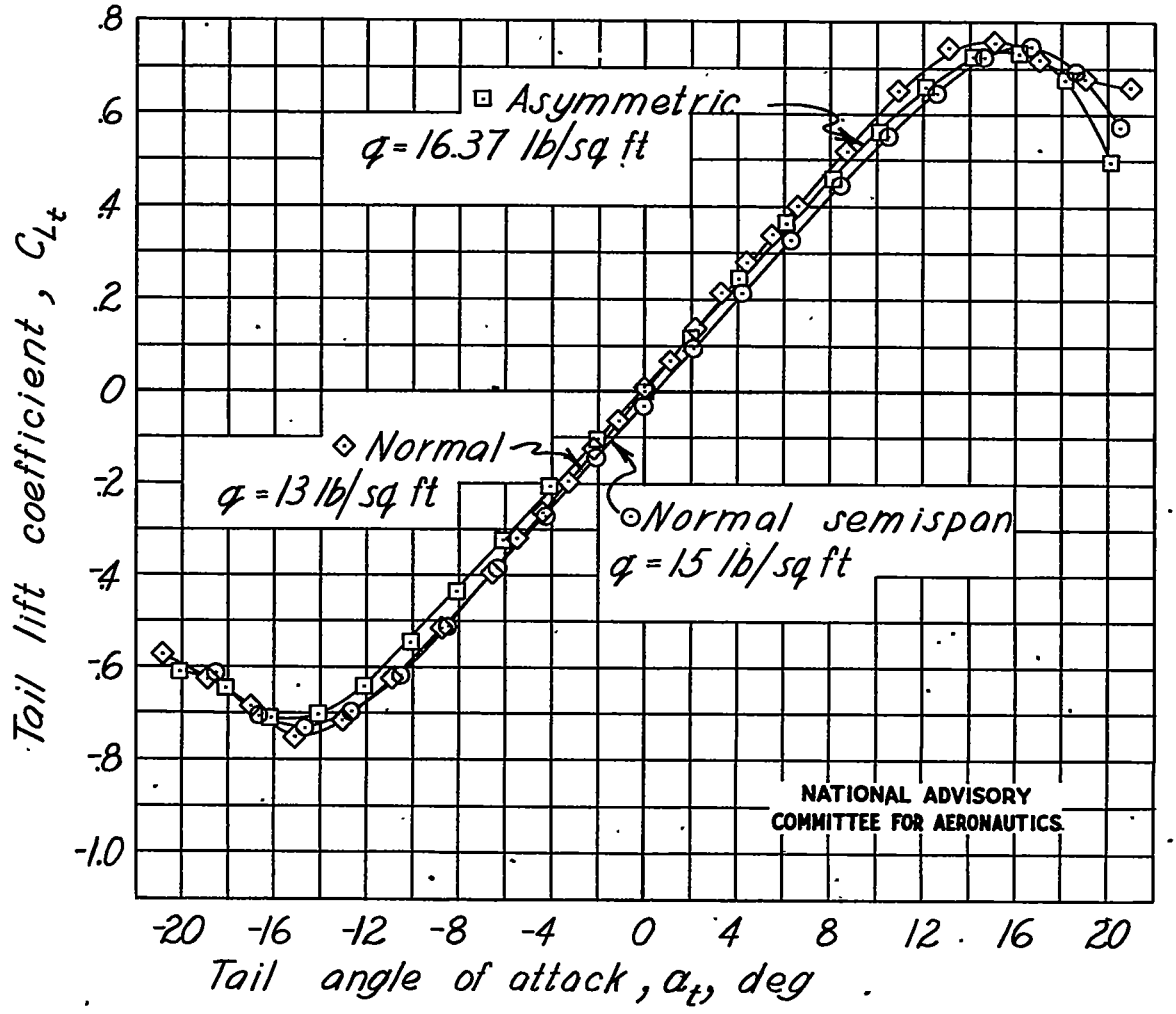

Figure 16.— Lift curves of the two horizontal tails used in tests of the single-engine low-wing airplane model.

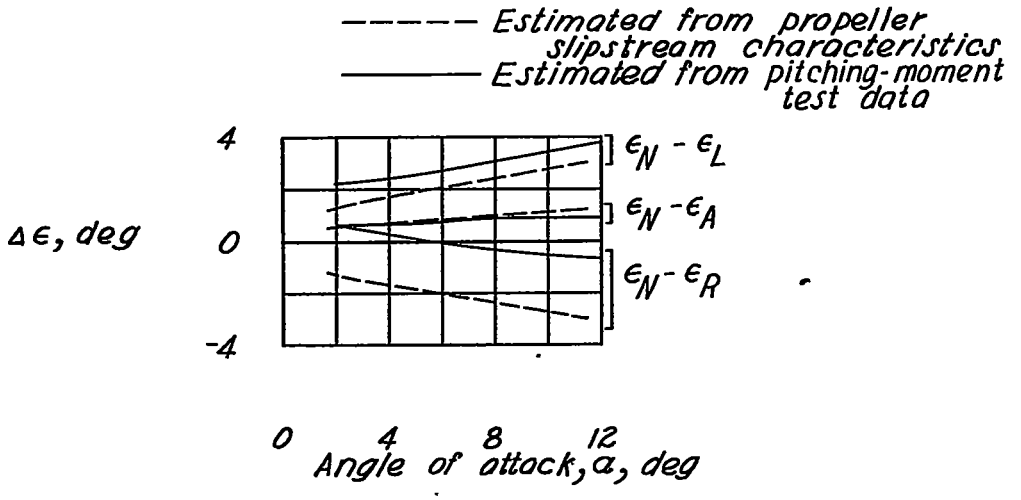

Figure 17.- Comparison of values of change in downwash angle $\Delta\epsilon$ due to horizontal-tail arrangements of the single-engine airplane model. $\delta_f = 0°$; $q = 16.37$ pounds per square foot; power on; N, normal tail; L, left semispan of normal tail; R, right semispan of normal tail; A, asymmetric tail.

NATIONAL ADVISORY
COMMITTEE FOR AERONAUTICS

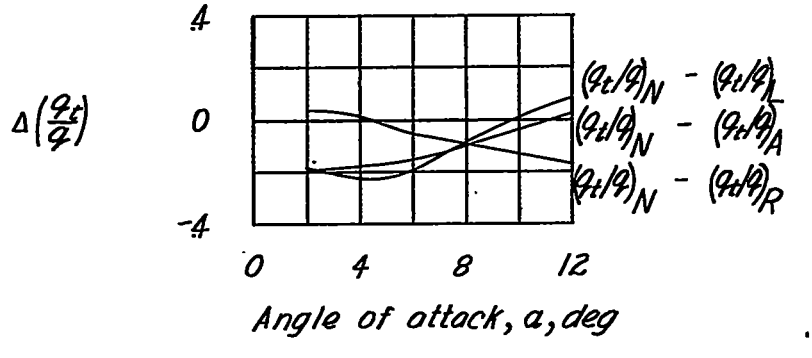

NATIONAL ADVISORY
COMMITTEE FOR AERONAUTICS

Figure 18.- Comparison of values of change in dynamic-pressure ratio $\Delta(q_t/q)$ due to horizontal-tail arrangements of the single-engine airplane model. $\delta_f = 0°$; $q = 16.37$ pounds per square foot; power on; N, normal tail; L, left semispan of normal tail; R, right semispan of normal tail; A, asymmetric tail.

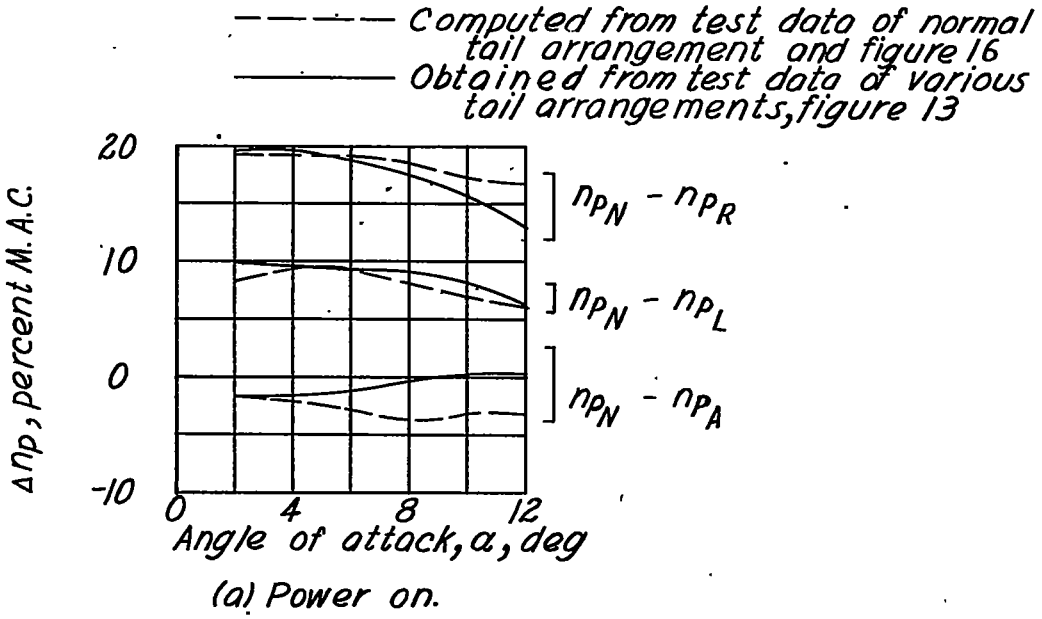

(a) Power on.

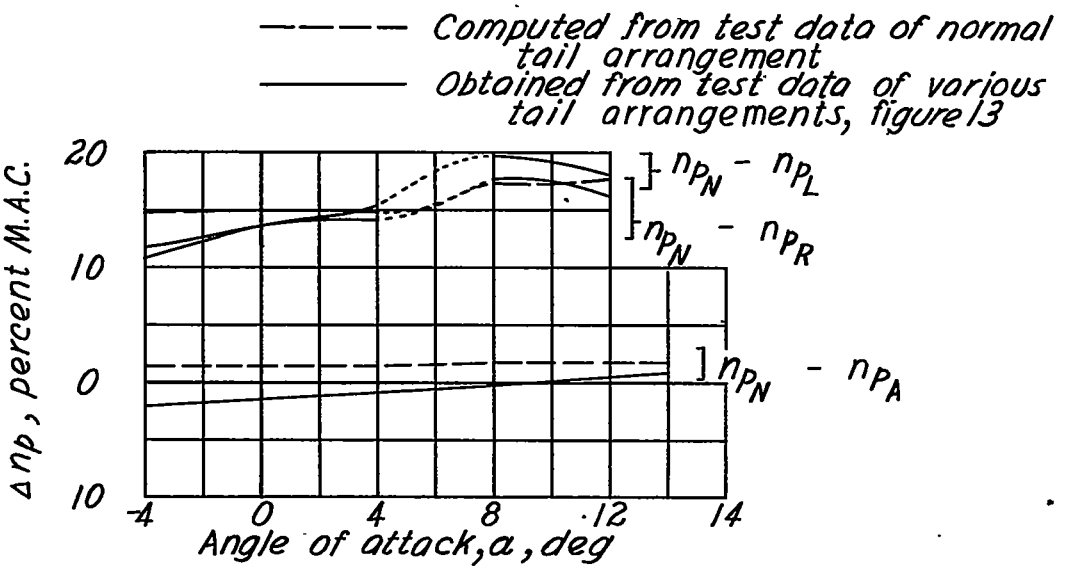

NATIONAL ADVISORY COMMITTEE FOR AERONAUTICS

(b) Power off.

Figure 19.- Comparison of values of change in computed neutral-point location Δn_p due to horizontal-tail arrangements of the single-engine airplane model. $\delta_f = 0°$; $q = 16.37$ pounds per square foot; N, normal tail; L, left semispan of normal tail; R, right semispan of normal tail; A, asymmetric tail.

(a) $\delta_f = 0°$; windmilling propeller.

(b) $\delta_f = 0°$; power on.

NATIONAL ADVISORY COMMITTEE FOR AERONAUTICS

Figure 20. – Effect of horizontal-tail arrangements on lateral forces and moments at zero yaw for the single-engine airplane model. N, normal tail; R, right semispan of normal tail; L, left semispan of normal tail; A, asymmetric tail.

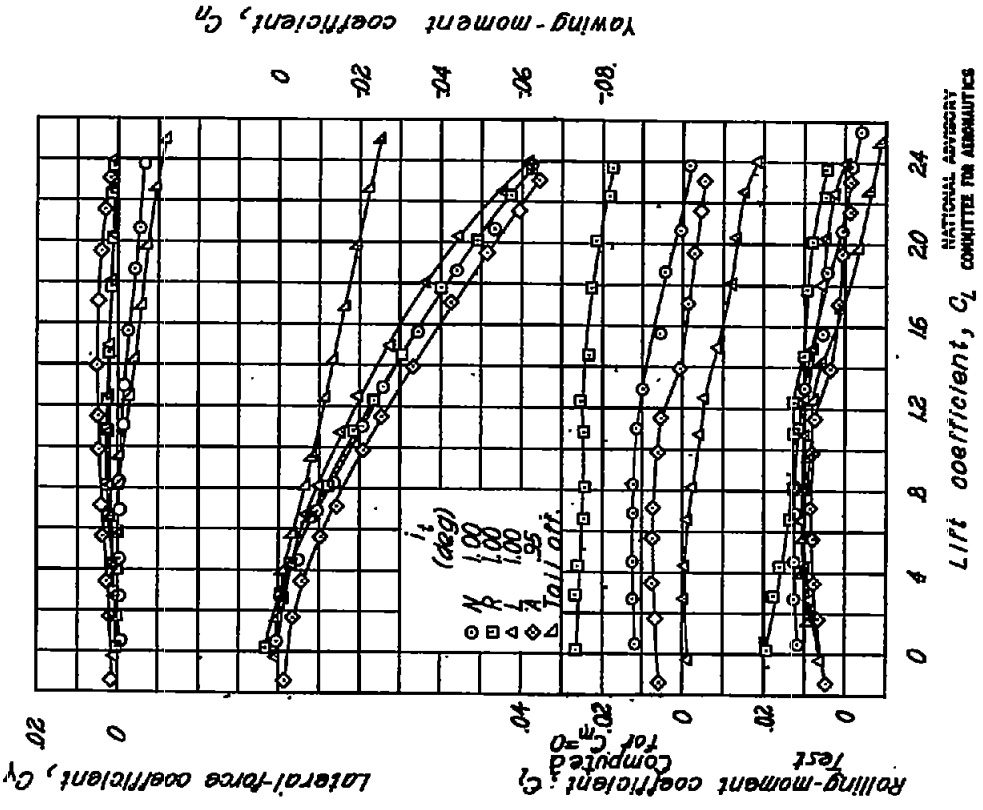

(d) $\delta_f = 37°$; power on.

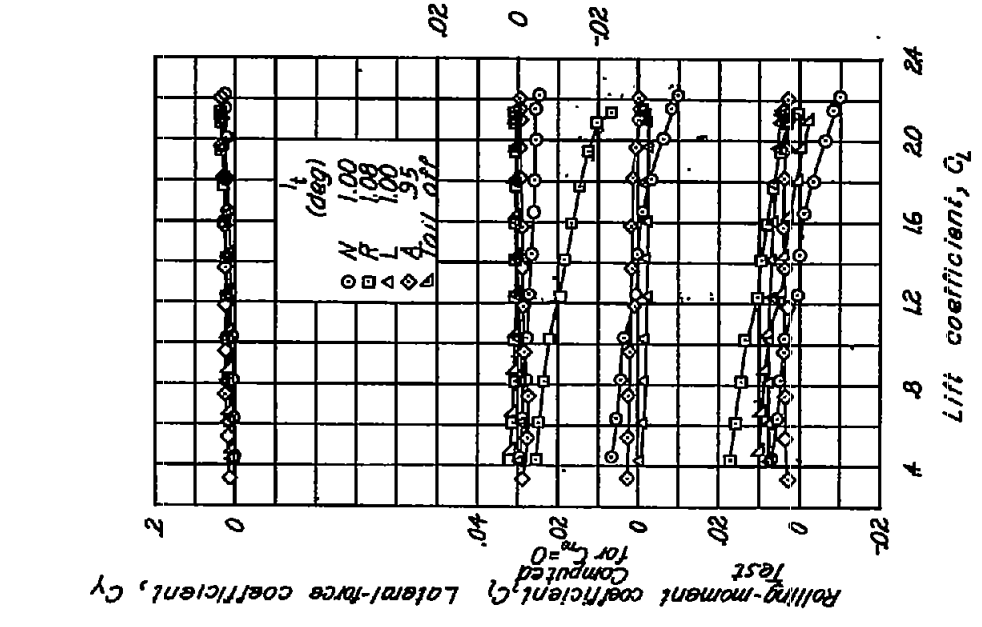

(c) $\delta_f = 37°$; windmilling propeller.

Figure 20.- Concluded.